Master's thesis
Atmospheric Chemistry & Analysis

Formation of ROR dimers from Peroxy Radical Recombination Reactions

Lauri Franzon

January 17, 2022

Supervisor(s): prof. Theo Kurten
prof. Mikael Ehn

Censor(s): doc. Arkke Eskola

UNIVERSITY OF HELSINKI
Master's Programme in Atmospheric Sciences

HELSINGIN YLIOPISTO — HELSINGFORS UNIVERSITET — UNIVERSITY OF HELSINKI

Tiedekunta — Fakultet — Faculty	Koulutusohjelma — Utbildningsprogram — Education programme
Faculty of Science	Master's Programme in Atmospheric Sciences

Tekijä — Författare — Author
Lauri Franzon

Työn nimi — Arbetets titel — Title

Formation of ROR dimers from Peroxy Radical Recombination Reactions

Opintosuunta — Studieinriktning — Study track
Atmospheric Chemistry & Analysis

Työn laji — Arbetets art — Level	Aika — Datum — Month and year	Sivumäärä — Sidoantal — Number of pages
Master's thesis	January 17, 2022	79 pages

Tiivistelmä — Referat — Abstract

The oxidation mechanisms of atmospheric organic compounds are an important puzzle piece for many atmospherically relevant topics, including but not limited to air quality and climate change. One poorly understood step in this oxidation process is peroxy radical recombination, in some conditions the most important sink reaction for peroxy radicals, which are formed in abundance due to gas phase reactions in the lower troposphere.

After a few initial steps, the peroxy radical recombination reaction results in the ejection of O_2 leaving behind a pair of alkoxy radicals in close proximity. This reactive complex has three known reaction pathways: Hydrogen shift forming an alcohol and a carbonyl compound, radical recombination forming a ROOR dimer, and diffusive break-up forming two free alkoxy radicals. In this thesis, alkoxy bond scission followed by radical recombination resulting in the formation of a ROR is proposed as a fourth reaction pathway.

To test the hypothesis, computational chemistry was used to determine alkoxy bond scission rates for radicals of atmospheric significance, and gas-phase oxidation experiments were realized on three peroxy radical precursor molecules to look for signs of ROR formation. More precisely, the Eyring equation was used to calculate the rate of alkoxy bond scission on a potential energy surface determined using density functionals, with corrections to electronic energy using coupled-cluster calculations. In the experiments, liquid phase alkenes were vaporized, and oxidized by O_3 in the gas phase, resulting in peroxy radical formation, after which the possible dimers were detected using a NO_3^--atmospheric pressure chemical ionization time-of-flight mass spectrometer. A highly oxidized radical reaction partner was present in the chamber to improve the detectability of the formed dimers.

The combined results of these two approaches suggest that the reaction pathway is possible in standard atmospheric conditions and may thus be important for a number of peroxy radicals.

Avainsanat — Nyckelord — Keywords
Peroxy radical recombination, Alkoxy bond scission, Dimer formation, Computational, Experimental

Säilytyspaikka — Förvaringsställe — Where deposited

Muita tietoja — övriga uppgifter — Additional information

Contents

1. Introduction

Atmospheric aerosol particle dynamics is an important research subject in environmental physics as the particles have a crucial role in urban air quality as well as an important but notoriously difficult to quantify impact on climate change [1]. Aerosols are categorized into *primary* and *secondary* aerosol particles, the first of which enters the atmosphere in the particle phase and the latter of which forms in the atmosphere. Global atmospheric models have long disagreed with in situ measurements on the amount of aerosol mass consists of the latter, implying there are plenty of details in the mechanism of secondary aerosol formation which we are not yet fully aware of [2]. What we do know is that gas phase atmospheric chemistry plays a large part, as both the creation of new aerosol particles [3], and growth of newly formed secondary aerosol particles [4], depend of the presence of low-volatility compounds. One important class of atmospheric chemical compounds known for their low volatility are *Highly oxygenated organic molecules* (HOM), which is a collective name for sufficiently oxidized products of organic compounds that are emitted into the atmosphere from the surface [5]. This is in theory a very broad group of compounds, but the number of oxidation mechanism responsible for their formation in atmospheric conditions is limited. This thesis is primarily concerned with one such chemical reaction, namely peroxy radical recombination. There are three known products of this reaction (fully covered in Chapter 2), and our goal is to investigate whether a fourth, the formation of HOMs with the formula ROR, is possible. This topic is quite far into the specifics of

atmospheric chemistry, which means that we first have to cover the the general aspects of atmospheric chemistry.

Summed up in very general terms, atmospheric chemistry is the chemistry of oxidation. This is a consequence of the fact that 20,9% of the atmosphere is composed of molecular oxygen, which is next to highest in electronegativity among all the elements. As such, all reduced or partially reduced compounds emitted to the atmosphere from the surface will eventually end up oxidized. This in turn increases the amount of polar bonds in the compound, strengthening the intermolecular Coulomb interactions the compound takes part in. From a macroscopic point of view, this in turn leads to a decreased saturation vapour pressure, rendering the compound more likely to participate in nucleation mechanisms, condense on aerosol particle surfaces, or dissolve in water droplets. This is of course a very crude and idealized summary of Atmospheric Chemistry, but it does capture its most relevant processes in broad strokes. The science is of course in figuring out the details of said processes for each emitted compound: Which oxidation mechanisms are most likely, how stable the products are, and what are the most likely physical removal mechanisms for said products.

An important aspect of traditional organic chemistry is figuring out whether reactions are under *thermodynamic control* or *kinetic control*. The former generally applies in conditions in which all reactions go both ways, meaning that the most entropy-maximizing eventually dominates. The latter, on the other hand generally means that reactions are all one-way, meaning that the fastest reactions dominate. Atmospheric reactions are almost without exception under kinetic control. This is due to another general trend of atmospheric chemistry: The most important reactions in the atmosphere are very rapid chain radical reactions, which are usually initiated by stable molecules (such as NO_2, O_3 and HNO_2) being decomposed by solar radiation. This

results in the formation of very reactive radicals with a very large pool of *potential* reactions, of which maybe a handful are kinetically competitive. For this reason, Reaction Kinetics provides the main theoretical framework for evaluating atmospheric reaction pathways [6].

This brings us back to the topic of peroxy radical (or $ROO\cdot$ in typical organic chemistry notation) recombination, as we now have the means to explain why the reaction is important. They form in the atmosphere when an oxygen molecule recombines with a carbon-based radical. In tropospheric conditions, this is often the only kinetically competitive sink reaction for carbon based radicals due to the abundance of O_2. This, combined with the relative stability of $ROO\cdot$ compared to other radical species, means that these ought to be a common species in the lower troposphere, especially in areas with an abundance of volatile carbon compounds. As such, the recombination of two $ROO\cdot$ emerges as a probable sink reaction, and as we will see, the products of this reaction are large highly oxygenated organics with several saturation vapour pressure-lowering functionalities. The reaction is thus of great interest for aerosol particle dynamics and atmospheric chemistry. As we will also see, however, the reaction is quite complex. It has multiple competing products and includes several reaction steps which pose a challenge both for computational modelling and experimental determination. The aim of the research presented in this thesis was to combine computational and experimental work to examine whether this reaction has a fourth product pathway in addition to the three known ones, which brings us to the full detailed explanation of the chemical background.

2. Chemical Background

Before anything kinetics-related is discussed, we have to introduce a model. As such, let us briefly discuss the basic assumptions behind reaction kinetics. A chemical reaction consisting of several steps is generally assumed to be reducable into a series of one-step *elementary reactions*, which are either *unimolecular* or *bimolecular*, depending on the number of reactants. The rates of decay of these partaking reactants follows the following scheme:

$$\frac{\mathrm{d[A]}}{\mathrm{d}t} = -k_r[\mathrm{A}] \qquad\qquad \frac{\mathrm{d[A]}}{\mathrm{d}t} = -k_r[\mathrm{A}][\mathrm{B}] \tag{2.1}$$

Here k_r is a generic rate coefficient, denoted with r to distinguish it from the Boltzmann constant k. Note that k_r has the unit s^{-1} for unimolecular reactions and $\mathrm{s}^{-1}\left(\frac{\mathrm{cm}^3}{\mathrm{molec.}}\right)$ for bimolecular reactions. The simplest possible model for the dependence of k_r on reaction conditions is the Arrhenius equation, which only accounts for temperature-dependence, as that is the most significant variable affecting the rate of a generic elementary reaction:

$$k_r(T) = A\exp\left\{\frac{-E_A}{kT}\right\} \tag{2.2}$$

Here, A is the pre-exponential factor, a frequency corresponding to the rate of the reaction in conditions unrestricted by energy. E_A is the activation energy, roughly corresponding to the energy difference between the reactant molecule(s) and the energy saddle point between it and the product molecule(s). The Arrhenius equation is a very

simplified model, suitable mainly for rough estimation of the rates of fairly simple reactions. A somewhat more accurate model will be introduced in Chapter 4, but for the discussions in this chapter, Arrhenius suffices, as it accounts for one of the most fundamentals properties of reaction rates: the exponential dependence on thermal energy.

2.1 Formation of atmospheric peroxy radicals

Next, we will cover the reactions leading up to formation of $ROO\cdot$ in the atmosphere. All three of the most important atmospheric oxidants, the hydroxy radical ($OH\cdot$), the nitrate radical ($NO_3\cdot$) and Ozone (O_3), have at least one reaction pathway leading to formation of $ROO\cdot$. The first two of these can react with both alkanes and alkenes, whereas O_3 can only react with alkenes.

$OH\cdot$ adds to a C=C-double bond, initially forming a carbon-centered radical. The rate coefficient of the addition is in the range $(2{,}63 - 23) \cdot 10^{-11} \frac{\text{cm}^3}{\text{molec. s}}$ according to Atkinson et. al [7], depending mainly on the number of alkyl substituents. The observed trend is explained by the stability of the product radical. The more substituted the radical, the lower its barrier energy, and the faster the reaction. This radical goes on to react with molecular oxygen to form the peroxy radical. The rate of this reaction is around $k_r \geq 10^{-12} \frac{\text{cm}^3}{\text{molec. s}}$, which at an O_2 mixing ratio of 0,209 and a pressure of 1 atm translates to $k_r[O_2] \geq 5 \cdot 10^6$ s^{-1}. Some carbon-based radicals have unimolecular reactions faster than this, but for most cases one can assume that this is the dominant reaction. The reaction as a whole is summed up in Figure 2.1.

The $OH\cdot$ initiated oxidation of saturated hydrocarbons is somewhat slower, at $(1{,}44 - 18{,}3) \cdot 10^{-13} \frac{\text{cm}^3}{\text{molec. s}}$. The mechanism is roughly similar, the main difference being that the $R\cdot$-radical is formed through loss of a H atom (forming H_2O with the OH

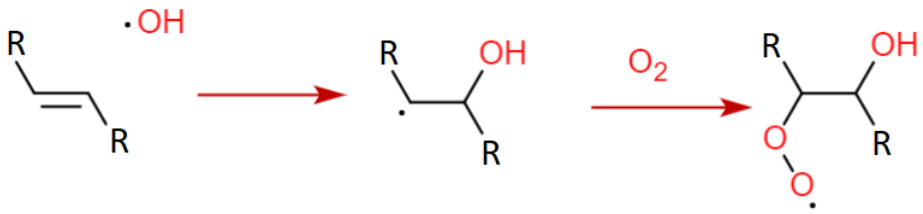

Figure 2.1: The mechanism of OH oxidation of alkenes, up until formation of the peroxy radical.

radical) instead of addition to the double bond. As such, unlike in OH· oxidation of alkenes, no new functionalities are gained besides the peroxy radical. This means that their products generally have higher saturation vapour pressures than the corresponding alkene-derived products, and are thus less likely to partake in HOM formation. These are thus, from our point of view, the least interesting kind of atmospheric peroxy radicals. As such, we will not be discussing these further in this thesis.

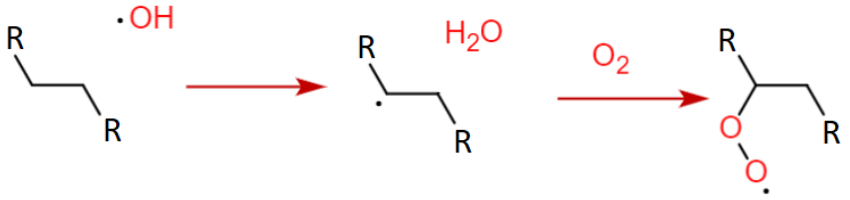

Figure 2.2: The mechanism of OH oxidation of alkanes, up until formation of the peroxy radical.

The chemistry of $NO_3\cdot$ is not far removed from the chemistry of OH·. The same addition and abstraction reactions occur, but instead of alcohols and water we get nitrate esters and nitric acid as products, respectively. The main difference lies perhaps in the kinetics of the reactions. The rate of the alkene addition reactions is in the range $(6{,}70 - 6850) \cdot 10^{-15} \frac{\text{cm}^3}{\text{molec. s}}$, while the rate of the alkane H-abstraction reaction is in the range $(1 - 100) \cdot 10^{-18} \frac{\text{cm}^3}{\text{molec. s}}$, [8]. Both reactions are significantly slower than those of OH·, and considerably more dependent of the presence of alkane and alkene substituents. Both observed trends are explained by the stability of the resonance

structure of the $NO_3\cdot$, rendering it less susceptible to addition reactions. Additionally, while the differences in barrier energies between the radical intermediates (ΔE_A) may be roughly the same as in the $OH\cdot$ case, the fact that the total energy barrier (E_A) is larger results in a larger spread of reaction rates, as seen from equation (2.2).

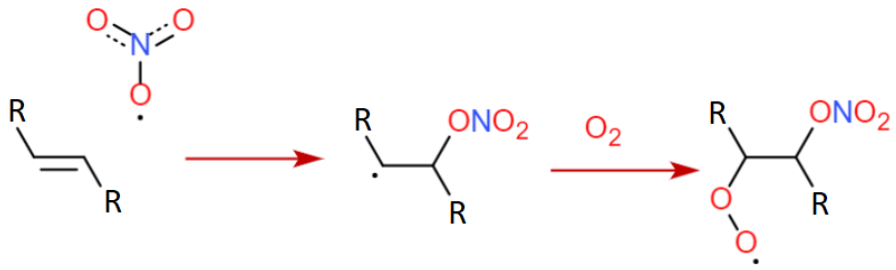

Figure 2.3: Oxidation mechanisms by NO_3

The formation of peroxy radicals from ozone oxidation is quite a bit more complex. To start with, it is specific for alkenes. It starts with the addition of the O_3 molecule to the double bond, forming an intermediate called a *primary ozonide* [9]. This primary ozonide decomposes into a carbonyl and a carbonyl oxide, a so-called *Criegee Intermediate*. In theory, the additional oxygen atom could go to either side of the former C=C-bond. Intramolecular interactions between the carbonyl oxide and other functional groups most likely have an impact, but we do not have sufficient quantitative data on the subject. The Criegee intermediate has two chemically significant conformers, a *syn*-conformer in which the oxide faces the carbon chain, and an *anti*-conformer where it doesn't. For the first of these, the most likely sink is an unimolecular H-shift forming an unstable [10] vinyl hydroperoxide, which decomposes into an OH radical and a carbon centered radical with a carbonyl functionality. This radical then forms peroxy radicals by the now familiar mechanism. This process is shown in Figure 2.4. The anti-conformer has different reactivity, and does not have any known significant peroxy radical forming pathways. On the same note, the unimolecular H-shift

isn't the most likely unimolecular reaction for all syn-conformer Criegee intermediates [11], meaning that all ozonolysis mechanisms do not eventually lead to formation of peroxy radicals.

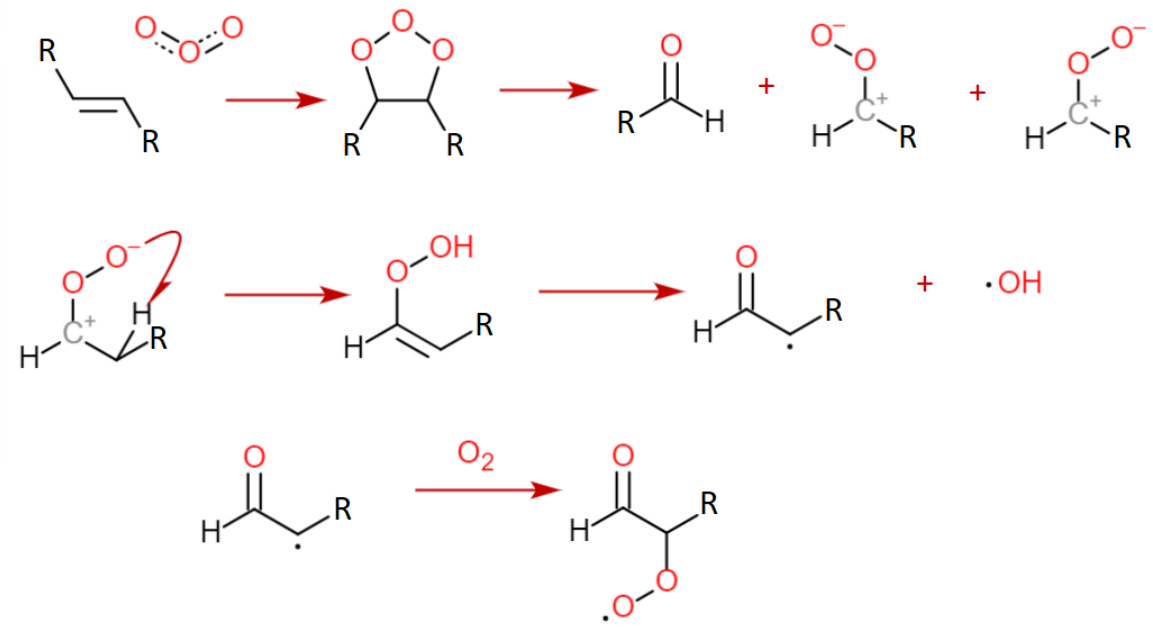

Figure 2.4: Formation of peroxy radicals from ozonolysis.

2.2 Competing reactions

Peroxy radical recombination is not the only possible reaction for the $ROO\cdot$, but it is a significant reaction. In this chapter, we will discuss the topic of peroxy radicals and peroxy radical recombination in detail, starting with the reason for why they are relatively stable. Unlike most atmospheric radicals, the $ROO\cdot$ radical center is lacking in low-barrier addition routes, leaving H-abstaction as the most likely unimolecular reaction pathway, which is slow in the most common cases [12]. Examples of rapid H-shifts do exist whenever acidic H atoms are present, but these reportedly result in the formation of carbon-centered radicals, and thus new $ROO\cdot$. When this happens unimolecularly, it is called *autoxidation*, and it is quite rapid in several cases [13]. A notable exception to this is the case shown in Figure 2.4, as vinyl hydroperoxides are not nearly as stable as hydroperoxides, but as has been established, that reaction pathway also results in $ROO\cdot$ formation [10]. In short, no commonly available unimolecular reactions lead to a net loss of $ROO\cdot$ groups. This means the most important sink reactions for peroxy radicals are recombination reactions with other radicals, the most atmospherically relevant of which are $NO_x\cdot$, $HO_2\cdot$, and of course, other $ROO\cdot$.

$$ROO\cdot + HO_2\cdot \longrightarrow ROOH + O_2 \tag{2.3a}$$

$$ROO\cdot + NO\cdot \longrightarrow RO\cdot + NO_2\cdot \tag{2.3b}$$

$$ROO\cdot + NO_2\cdot \longrightarrow ROONO_2 \longrightarrow P \tag{2.3c}$$

$$ROO\cdot + NO_3\cdot \longrightarrow RO\cdot + NO_2\cdot + O_2 \tag{2.3d}$$

The $NO_x\cdot$ class of reactions, particularly the $ROO\cdot + NO$ reaction, dominate the sink term of peroxy radicals in environments with moderate degrees of anthropogenic emissions. In less polluted environments, the $HO_2\cdot$ and $ROO\cdot$ are the two crucial reactions. The first has been found to have an experimental rate coefficient on the order of $k \approx 10^{-12}\ \mathrm{s}^{-1}\frac{\mathrm{cm}^3}{\mathrm{molec.}}$, while $ROO\cdot$ recombinations have a much broader range, from

$k \approx 10^{-11}$ s$^{-1}\frac{\text{cm}^3}{\text{molec.}}$ to $k \approx 10^{-17}$ s$^{-1}\frac{\text{cm}^3}{\text{molec.}}$, ultimately depending on the pair of peroxy radicals in question [14]. Field experiments show that the tropospheric concentration of $HO_2\cdot$ is on the order of $[HO_2\cdot] = 10^8\frac{\text{molec.}}{\text{cm}^3}$ [15]. This concentration is quite low, meaning that the $ROO\cdot$ recombination may very well overtake the $HO_2\cdot$ reaction in some conditions.

2.3 Mechanism of peroxy radical recombination

The mechanism of peroxy radical recombination was first proposed by K.U Ingold based on liquid phase laboratory experiments [16]. The first step of the reaction is the formation of an intermediate tetroxide structure, from which the middle two O atoms then dissociate irreversibly, forming an O_2 molecule and two alkoxy radicals. These two radicals form a reactive complex, which may either react further or diffuse away. In the notation used in this thesis, this reactive complex will be noted using a parenthesis.

$$ROO\cdot + ROO\cdot \longleftrightarrow RO_4R \longleftrightarrow RO\text{---}O_2\text{---}OR \longrightarrow (RO\cdot + RO\cdot) + O_2 \qquad (2.4)$$

Later, Russell proposed a mechanism for the dissociation following the tetroxide formation in which a hydrogen shift from one peroxy carbon to the other results in the formation of an alcohol and an aldehyde [17]. This hypothesis was based on the fact that the total reaction rate was much faster for primary and secondary $ROO\cdot$ compared to tertiary $ROO\cdot$. He postulated a cyclic transition state composed of the four tetroxide oxygens, the two α-carbons and the shifting hydrogen atom. However, later experimental studies proved inconsistent with this mechanism [18], and according to the now accepted mechanism, the O_2 loss preceeds the hydrogen shift rather than the other way around [19]. All three known products of peroxy radical recombination

following the tetroxide dissociation are thus presented in equation 2.5.

$$(\mathrm{H{-}RO}\cdot + \mathrm{RO}\cdot) \longrightarrow \mathrm{ROH} + \mathrm{R{=}O} + \mathrm{O_2} \tag{2.5a}$$

$$(\mathrm{RO}\cdot + \mathrm{RO}\cdot) + \mathrm{O_2} \longrightarrow \mathrm{ROOR} + \mathrm{O_2} \tag{2.5b}$$

$$(\mathrm{RO}\cdot + \mathrm{RO}\cdot) + \mathrm{O_2} \longrightarrow \mathrm{RO}\cdot + \mathrm{RO}\cdot + \mathrm{O_2} \tag{2.5c}$$

Based on an earlier review by Orlando, Tyndall, & Wallington, the two most likely reactions for generic alkoxy radicals are unimolecular decomposition and reaction with O_2 [20]. The rate of the latter reaction is around $k = 10^{-14} \frac{\mathrm{cm}^3}{\mathrm{molec.\ s}}$ for the simplest alkoxy radicals, which translates to $k[\mathrm{O_2}] = 10^5\ \mathrm{s}^{-1}$ [21]. For most alkoxy radicals, this is uncompetitive compared to unimolecular decomposition. The decomposition reaction in question is an *alkoxy bond scission*, producing a carbon centered radical and a ketone. It is pictured in Figure 2.5. Reaction channels other than decomposition and reaction with O_2 (e.g. unimolecular isomerization) also exist, but are seldom the dominant sink for alkoxy radicals in atmospheric conditions.

Figure 2.5: The mechanism of alkoxy bond scission. As shown in the figure, the carbon atom bonded to the alkoxy radical is referred to as the α-carbon, whereas the carbon atom receiving the radical after the scission is referred to as the β-carbon.

As we will see, the alkoxy bond scission is not only fast enough to compete with the reaction with O_2, but also fast enough to compete with diffusion. Our proposal is that this reaction is fast enough to result in a fourth possible reaction pathway: Recombination of the carbon-centered radical with the unscissioned alkoxy radical, forming a ROR dimer. This theory would be consistent with experimental findings

that increasing the temperature results in a decrease of the products of 2.5a and 2.5b, at least for methyl peroxy radicals [22].

$$(\mathrm{RO}\cdot + \mathrm{RO}\cdot) \longrightarrow (\mathrm{R}'\cdot + \mathrm{RO}\cdot) + \mathrm{P} \longrightarrow \mathrm{ROR}' + \mathrm{P} \tag{2.6}$$

Here, we are using an apostrophe ($'$) to signify that the size of the carbon chain has been diminished due to alkoxy bond scission. This notation will remain consistent throughout the rest of the text. Now, let us go through what is currently known of all other aspects of the reaction, to determinate in which cases ROR formation is plausible.

The total decay rate of peroxy radicals caused by the $\mathrm{ROO}\cdot + \mathrm{ROO}\cdot$ has already been established to be of order $k \approx 10^{-11}$ $\mathrm{s}^{-1}\frac{\mathrm{cm}^3}{\mathrm{molec.}}$ to $k \approx 10^{-17}$ $\mathrm{s}^{-1}\frac{\mathrm{cm}^3}{\mathrm{molec.}}$ depending on the specific pair of $\mathrm{ROO}\cdot$. Ghigo et.al. derived an activation barrier of 21 kJ/mol for the decomposition of the tetroxide barrier, with the Arrhenius equation transtates to the same order of magnitude as the bimolecular collision limit. for the $\mathrm{MetOO}\cdot + \mathrm{MetOO}\cdot$ recombination [23]. This implies that the encounter of the two radicals is the rate-limiting step, at least in this case. However, Khursan derived activation barriers on the order of 40 kJ/mol for tetroxides formed from sec-$\mathrm{ROO}\cdot$ based on kinetic and thermodynamic experimental data of recombination reactions [24], which may explain part of the variance in the experimental kinetic data.

Once the tetroxide structure does fall apart, the three competing reaction pathways presented in equation 2.5 are all quite rapid. We will now cover these mechanisms one by one.

2.3.1 Hydrogen Shift forming ROH and R=O

Reaction 2.5a relies on a hydrogen shift from one R to the other before the dissociation of the RO---O_2---OR complex. Laboratory experiments [14] and theoretical studies [23]

both indicate that this is the dominant reaction pathway for the simplest possible recombination reaction, $CH_3OO\cdot + CH_3OO\cdot$, and significant for most other simple alkyl peroxy radicals. A computational study by Lee *et. al.* found that hydrogen bonding from both α- and β-carbons have a role in stabilizing the transition state of the H-shift, meaning that pathway 2.5a is even more likely for secondary peroxy radicals than it is for primary $ROO\cdot$ (For tertiary $ROO\cdot$, the pathway obviously isn't available due to the lack of H-atoms attached to the α-carbon)[19]. This observation forms an excellent rule-of-thumb for evaluating for which molecules the H-shift is a significant sink reaction.

2.3.2 Intersystem Crossing forming ROOR

Pathway 2.5b, resulting in the formation of an ROOR dimer, is somewhat more complicated, as it is dependent on a spin flip reaction. Let us therefore review the conservation of angular momentum and spin in chemistry. The total angular momentum of an electron has two components. Orbital angular momentum $\vec{l}$ and spin $\vec{s}$. Both are quantized, orbital angular momentum having values of $\vec{l} = \sqrt{l(l+1)}\hbar$, the quantum number l taking integer values starting from 0. The same is true for the spin vector, except that the quantum number s can (for an electron) only take two values, $s = +\frac{1}{2}$ and $s = -\frac{1}{2}$. In a system consisting of several electrons, these add up like a vector sum. The total spin for a system consisting of N electrons, commonly referred to as *spin multiplicity* by chemists, can take on the values:

$$\vec{S} = \Big|\sum_{i}^{N} \vec{s_i}\Big| = \hbar\left[\frac{N}{2},|\frac{N}{2}-1|,|\frac{N}{2}-2|,...\right] \tag{2.7}$$

and the same is true for the orbital angular momenta sum L, maximum value being $\vec{L} = \sum_i^N |\vec{l_i}|$. Note that the orbital angular momentum and spin multiplicity

vectors add up into the *total angular momentum* $\vec{J}$ [25] :

$$\vec{J} = \vec{L} + \vec{S} \tag{2.8}$$

If total spin is conserved in a chemical reaction ($\Delta\vec{S} = 0$), the reaction is *spin-allowed*. If not, the reaction is *spin-forbidden*. This terminology is not important for most generic chemical reactions, because most molecules are singlets ($\sum s = 0$) in their ground state, rendering the rules of spin conservation quite trivial. However, the oxygen molecule is a triplet ($\sum s = 1$) in its ground state, and this has consequences for ROOR formation. The fact that the O_2 dissociating from the RO---O_2---OR complex must be in a triplet state puts constraints on what spins the formed $RO\cdot$ might have. Four relevant highest occupied molecular orbitals electrons partake in the reaction step: Two in the O_2 molecule and one each in the $RO\cdot$. If the Tetroxide is in singlet state, then two of these electrons must have $s = +\frac{1}{2}$ and two $s = -\frac{1}{2}$. If the formed O_2 is to be a triplet, then the two remaining electrons must have equal spins. This means that the ROOR recombines as a triplet, which is thermodynamically unfavourable [26], or performs an *Intersystem Crossing* (ISC) into a singlet state. This is visualised using the spin-arrow notation common in chemistry in Figure 2.6.

This is where the total angular momentum comes in. Spin-forbidden reactions require an ISC to take place, and this means that spin is exchanged with orbital angular momentum, such that $\Delta\vec{S} = -\Delta\vec{L}$ and $\Delta\vec{J} = 0$. This requires a strong *spin-orbit coupling*, and the rate of the ISC thus depends on the strength of that coupling [27].

As for the calculation of ISC rates for the ($RO\cdot + \cdot OR$) system, Valiev *et.al.* derived a model for calculation of ISC rates based on quantum mechanical first principles, requiring quantum chemical calculations on several electronic and vibronic properties of both spin states [28]. The model will not be covered here, as it is beyond the scope

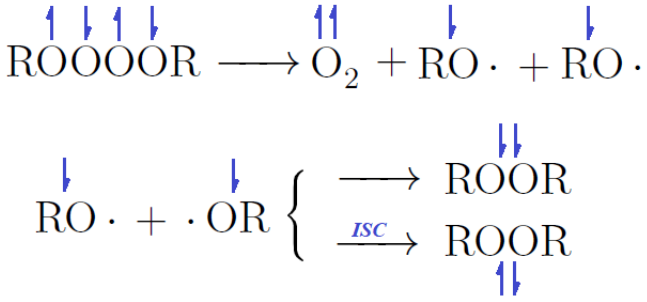

Figure 2.6: Visualisation of the spin conservation during pathway 2.4b of the peroxy radical recombination reaction. Alternatively, O_2 can form in is excited singlet state, meaning ($RO\cdot + \cdot OR$) is a singlet as well, thus requiring no ISC. This pathway was however found to be thermodynamically unfavourable by Ghigo *et.al* [23]

of this theses. The model has already been successfully applied on the $RO\cdot + \cdot OR$ system [26], with promising results, yielding rates between $k_{ISC} = 4 * 10^8$ s^{-1} and $k_{ISC} = 5 * 10^{12}$ s^{-1} for a small set of common alkoxy pairs. Comparison of these rates to those of the 2.5a pathway suggests that ISC to the singlet surface is indeed the mechanism with which the experimentally observed ROOR products are formed in the atmosphere [29].

2.3.3 Diffusion forming free $RO\cdot$

Experimental studies suggest that at least part of the formed alkoxy radicals are lost to diffusion, but the amount is difficult to quantify due to the reactivity of alkoxy radicals and the multitude of potential products [14]. In this chapter, we will derive a (crude) mathematical model of our own to quantify the extent of diffusive loss. A classical textbook model for diffusion-controlled reactions is constructed assuming the limiting factor for a reaction is the diffusion of reactants A and B towards each other [30]. In our system, the opposite is true: Our two reactants, the alkoxy radicals, are part of the same reactive complex upon formation, and they may either react immediately following formation of diffuse, breaking the reactive complex. The reaction in its entirety can as

such be expressed as:

$$\mathrm{RO_4R} \longrightarrow (\mathrm{RO}\cdot + \mathrm{RO}\cdot) \rightleftharpoons 2\mathrm{RO}\cdot \qquad\qquad (\mathrm{RO}\cdot + \mathrm{RO}\cdot) \longrightarrow \mathrm{P}$$

To simplify our notation, we will refer to $(\mathrm{RO}\cdot + \mathrm{RO}\cdot)$ as RC for 'reactive complex' in the following few equations. The time-dependence of [RC] can thus be expressed:

$$\frac{\mathrm{d[RC]}}{\mathrm{d}t} = k_{dis}[\mathrm{RO_4R}] + k_d[\mathrm{RO}\cdot]^2 - k'_d[\mathrm{RC}] - k_r[\mathrm{RC}] \tag{2.9}$$

where $k_{dis}[\mathrm{RO_4R}]$ is the dissociation rate of the tetroxide and $k_r[\mathrm{RC}]$ is the total reactivity of RC. $k_d[\mathrm{RO}\cdot]^2$ and $k'_d[\mathrm{RC}]$ are the rates of formation and breaking of the reactive complex by diffusion, the first of which is practically zero due to the high reactivity of alkoxy radicals. That said k'_d is the value we are primarily interested in, as it competes with k_r, our main subject of interest. Let us derive a value for it assuming diffusion from a point source as our physical model:

$$[\mathrm{RO}\cdot](r,t) = \frac{[\mathrm{RO}\cdot]_0}{8(\pi D t)^{\frac{3}{2}}} \exp\left\{-\frac{r^2}{4Dt}\right\} \tag{2.10}$$

where $[\mathrm{RO}\cdot]_0$ is the concentration integrated over all space and D is the diffusion constant. r and t are defined in relation to some source of diffusing particles, which is our case means the location and time of the O_2 ejection from the tetroxide. For the next step, let us assume there exists a limiting 'reactive radius' R past which the alkoxy radicals are no longer able to react with each other. Integrating the flux $(\vec{j})$ derived from Fick's first law [31] over a spherical surface gives us the rate of radicals diffusing out of R:

$$\oint_A \vec{j}_R \cdot \mathrm{d}A = R^2 \int \sin\theta \mathrm{d}\theta \int \mathrm{d}\phi \cdot D \frac{\partial[\mathrm{RO}\cdot]}{\partial r}|_R = -\frac{[\mathrm{RO}\cdot]_0 R^3}{4\pi^{\frac{1}{2}} D^{\frac{3}{2}} t^{\frac{5}{2}}} \exp\left\{-\frac{R^2}{4Dt}\right\} \tag{2.11}$$

which directly implies:

$$k'_d = \frac{R^3}{4\pi^{\frac{1}{2}} D^{\frac{3}{2}} t^{\frac{5}{2}}} \exp\left\{-\frac{R^2}{4Dt}\right\} \tag{2.12}$$

Turns out k'_d isn't a coefficient at all, but a time-dependent variable. In order to compare the diffusion rate to the competing reaction rates, we need a constant, and thus have to average k'_d over some time-scale. The most sensible way is probably by derive a half-life τ_d and then calculate the average diffusion rate using $\langle k'_d \rangle = \frac{\ln 2}{\tau_d}$.

$$\frac{1}{2} = \int_0^\tau k'_d \mathrm{d}t = 1 + \frac{R}{\sqrt{\pi D \tau}} \exp\left\{-\frac{R^2}{4D\tau}\right\} - \mathrm{erf}\{\frac{R}{2\sqrt{D\tau}}\}$$

$$\tau = -\frac{R^2}{2DW\{-\frac{\pi}{8}\left(4\mathrm{erf}\{\frac{R}{2\sqrt{D\tau}}\}^2 - 4\mathrm{erf}\{\frac{R}{2\sqrt{D\tau}}\} + 1\right)\}}$$

A most complex non-linear equation indeed, including not one but two special functions, the error function erf and the Lambert product logarithm W. We are not interested in the analytical solution, however, so we can solve it numerically for suitable input parameters for D and R. For the reactive radius, we select an arbitrary but believable value for radical recombination reactions, $R = 8 * 10^{-10}$m, whereas for the diffusion constant, we use a known result from kinetic gas theory:

$$D = \frac{1}{3}\lambda\langle v \rangle = \frac{1}{3}\frac{\eta}{p}\sqrt{\frac{\pi kT}{2m}}\sqrt{\frac{8kT}{\pi m}} = \frac{2\eta kT}{3pm} \tag{2.13}$$

At the viscosity of air $\eta = 1{,}85 \cdot 10^{-5} \frac{\mathrm{kg}}{\mathrm{m\ s}}$, normal atmospheric conditions $p = 1$ atm, $T = 300$ K and mass $m = 59{,}044$ amu $= 9{,}8047 \cdot 10^{-26}$ kg (This is the mass of the lightest alkoxy radical of interest, $C_2H_3O_2\cdot$), gives the value $D = 5 * 10^{-6} \frac{\mathrm{m}^2}{\mathrm{s}}$. These values give us a half-life og $\tau \approx 6{,}08 * 10^{-13}$ s. This results in the following average diffusion rate:

$$\langle k'_d \rangle = \frac{\ln 2}{\tau_d} \approx 1 * 10^{12}\ \mathrm{s}^{-1}$$

As we will see in later chapters, this value is most certainly fast enough to effectively compete with the reactions of the $(\mathrm{RO}\cdot + \mathrm{RO}\cdot)$ complex. More massive radicals

diffuse slower, as seen in equation 2.13, rendering the reactions more competitive.

Assuming this model is roughly accurate, the yield (Φ) of alkoxy radicals lost to diffusion can be calculated with the following equation:

$$\Phi_d \approx \frac{\langle k'_d \rangle}{k_H + k_{ISC} + k_S + \langle k'_d \rangle} \tag{2.14}$$

This does come with some disclaimers, however, as the simplifying assumptions made in the model might turn out to be significant:

1. The binding energy of the radicals is neglected. In reality, the radicals are bound by some potential $V(r)$, decreasing the diffusion rate. The magnitude of this potential depends on the presence of alkoxy substituents, and may not be negligible [29].

2. The Maxwell-Boltzmann mean speed $\langle v \rangle$ does not take into account any excess kinetic energy the radicals may have due to the exothermicity of the tetroxide dissociation

3. Being physically close enough to recombine (Here somewhat arbitrarily chosen as $2R_H$) may not suffice if the radicals are already rapidly heading in the opposite directions.

4. The alkoxy bond scission reaction may not directly lead to recombination of $\mathrm{RO}\cdot$ and $\mathrm{R}'\cdot$, due to reason 2.

Taken together, all of these suggest that Φ_d may be larger or smaller than suggested by equation 2.14 in reality, depending on the steepness of $V(r)$. Then again, $k'_d \propto t^{-\frac{5}{2}}$ applies past the half-life, so our method of determining the average $\langle k'_d \rangle$ may well overestimate the diffusive yield. Either way the model is only good for order of magnitude estimation.

Finally, for the fraction of alkoxy radicals escaping the reactive complex, the most likely atmospheric pathway is eventual reaction with oxygen, possibly preceded by a rapid unimolecular reaction. In the case of alkoxy bond scission:

$$\mathrm{RO}\cdot \longrightarrow \mathrm{R}'\cdot + \mathrm{P} \qquad\qquad \mathrm{R}'\cdot + \mathrm{O}_2 \longrightarrow \mathrm{R}'\mathrm{OO}\cdot \tag{2.15}$$

Now, what have we learned from this endeavour? We have learned that, according to our current best estimates, the peroxy radical recombination reaction has four possible products all of which follow the breaking of the tetroxide complex, as shown in equations 2.5 and 2.6. Of these, the diffusive loss k'_d is most likely always competitive, the hydrogen shift k_H may be competitive depending on the availability of suitable groups, k_{ISC} is competitive with suitable spin-orbit interaction in the radicals, and k_S is competitive if the alkoxy bond scission is fast, presuming that this is indeed what drives ROR′ formation. Out of these four, k_{ISC} is the most complex to calculate, and will likely be the last puzzle piece to be filled. Summing up all of the product yields into a series of equations:

$$\Phi_{\mathrm{ROH}} = \frac{k_H}{k_H + k_{ISC} + k_S + \langle k'_d \rangle} \tag{2.16a}$$

$$\Phi_{\mathrm{ROOR}} = \frac{k_{ISC}}{k_H + k_{ISC} + k_S + \langle k'_d \rangle} \tag{2.16b}$$

$$\Phi_{\mathrm{ROR}'} = \frac{k_S}{k_H + k_{ISC} + k_S + \langle k'_d \rangle} \tag{2.16c}$$

We will be using these assumptions to interpret our experimental data in Chapter 5.

3. Methodology

A combination of computational and experimental methods was used to investigate the formation of ROR′ dimers. In this chapter, we will briefly discuss why this combination of methods was chosen without going too much into detail on the specifics of either. Ultimately, it comes down to the overwhelming difference in computational complexity required for determining the rate of alkoxy bond scission and the rate of primary competitor, the ISC-driven dimerisation.

Alkoxy bond scission reactions are a relatively simple system to solve for computationally, as far as quantum chemical calculations go. The reaction coordinate is quite simple to find in configuration space, as it simply corresponds to a bond stretch along the breaking chemical bond. Furthermore, energy optimisation computations are cheap as long as the alkoxy radicals are relatively small, and energy optimisations for products are naturally even cheaper. As such, solving for k_S is a problem easily implementable by quantum chemical calculations.

On the other hand, k_{ISC} depends on relativistic quantum effects, and those are quite a bit more complex to solve for computationally. The computational method used by Valiev *et.al.* briefly mentioned in Chapter 2 requires solving for the energies of all spin states that may or may not contribute to the ISC, as well as spin-orbit coupling and non-adiabatic coupling perturbation operators for all interactions between

spin states. Multi-reference methods are a requirement due to the spin-complexity of the system. All in all, this means a considerable amount of computations (on systems twice the size of the corresponding alkoxy radicals, no less) have to be implemented for the calculation of one k_{ISC}. This takes time, effort, and computational resources. This means that comparing k_S and k_{ISC} on a purely computational level is a highly resource-intensive method of investigation.

On the other hand, taking the experimental approach allows one to simply implement the recombination reaction and measure the quantity of formed ROOR and ROR′, assuming both are detected. This will allow us to determine if fast alkoxy bond scissions accurately predict formation of ROR′, and if the signals are good enough, the method might even be used to determine an experimental value for the quotient of k_{ISC} and k_S.

The computational part of the research (fully detailed in Chapter 4) were started by implementing Vereecken's & Peeters's Structure-Activity Relationship [32] on a number of atmospherically relevant systems that could realistically be experimentally oxidized and measured. Quantum chemical computations were implemented for select systems for more accurate k_S rate determination. Based on these computational results, a small number of alkenes forming a conveniently limited number of peroxy radicals with competitive bond scission reactions were chosen for experimental studies (fully detailed in Chapter 5). The computations were all implemented using the Gaussian quantum chemistry program suite on the Puhti cluster of the CSC Data Center situated in Kajaani in Northern Finland. All experiments were performed in the Comprehensive molecular characterization of secondary organic aerosol formation in the atmosphere Laboratory (COALA in short), situated at premises of The University of Helsinki.

4. Computational Studies

4.1 Theory of Computational Methods

Kinetics of the most relevant alkoxy bond scissions reactions were investigated using quantum chemistry, in which the basic idea is to solve the Schrödinger Equation numerically for a chemical system, and model the *Potential Energy Surface* for said system in $3N$-dimensional configuration space (essentially $V(q_1, q_2, ..., q_{3N})$, where each general coordinate q_i refers to the motion of an atom along an axis). Our goal is to find the *reaction coordinate*, the trajectory in configuration space corresponding to the reaction of interest, in our case the alkoxy bond scission. The kinetic energy of the molecule naturally has an impact on the reaction rate as well, and this was calculated using statistical mechanics, essentially by modelling the rate at which the energy of the reactant fluctuates specifically along the reaction coordinate. This is expressed by the Eyring equation.

4.1.1 The Eyring Equation

Computational rate coefficients were calculated using the Eyring Equation [30]:

$$k_S = \kappa \frac{kT}{h} \frac{Q_{TS}}{Q_R} \exp\left\{ \frac{E_R - E_{TS}}{kT} \right\} \tag{4.1}$$

where R refers to the reactant and TS refers to the Transition state. In the equation, $\frac{kT}{h}$ expresses the rate of energy fluctuation as a function of temperature (as you see, the unit is number of energy quanta per second), $\frac{Q_{TS}}{Q_R}$ is a quotient of statistical partition

functions functioning as a statistical weight to said fluctuation, and the exponential factor expresses the fraction of reactant molecules with enough energy to ascend the energy barrier $E_{TS} - E_R$, as is usual in reaction kinetics.

κ is a factor accounting for the effect of quantum tunnelling may have on the rate of the reaction. The model chosen for this is Eckart's solution to the Schrödinger Equation for an unsymmetrical potential [33], as it is the most accurate tunnelling model which can be calculated separately without additional quantum chemical optimisations. We will not cover the derivation of this model in full detail, as the model was barely used in our calculations, but the full equation for the tunnelling factor is:

$$\kappa = \frac{\exp\left\{\frac{E_R}{kT}\right\}}{kT} \int_0^\infty \Gamma(E) \exp\left\{-\frac{E}{kT}\right\} \mathrm{d}E \tag{4.2}$$

Where $\Gamma(E)$ is a so called *reflection coefficient* dependent of the geometry of the reaction coordinate. The reason that this relatively simple model was that tunnelling probabilities are typically quite low for any system dependent on heavy atom (which on a quantum scale refers to anything heavier than Helium) movement, and alkoxy bond scissions depend on C-C -vibrations. One sanity check calculation was performed on the $C_2H_3O_2\cdot$ bond scission with the result $\kappa = 1{,}06$. As tunnelling is less likely in heavier systems, κ was assumed to be lower for all other reactions. It was thus neglected with good conscience. Accordingly, all results presented in Chapter 4.4. assume $\kappa \approx 1$.

4.1.2 Molecular Energies

Since we are neglecting tunnelling effects, Equation 4.1 includes four variables that are determined using quantum chemistry: E_R, E_{TS}, Q_R, and Q_{TS}. Before any detail is shed on specific calculations, we will shortly cover the theory on what these energies and partition functions are made up of. The total energy of a molecule can be split into four components: Electronic Energy, the kinetic and potential energy of the electrons,

Vibrational energy, the kinetic and potential energy of the nuclei relative to their equilibrium position, and Rotational and Translational Energy, the kinetic energy of the entire molecule moving at once. It can thus be summed up as:

$$E_{tot} = E_e + E_v + E_r + E_t \tag{4.3}$$

Statistical partition functions Q are defined as follows:

$$Q \equiv \int \exp\left\{-\frac{E}{kT}\right\} \mathrm{d}\Gamma = \sum_{i=0}^{\infty} g_i \exp\left\{-\frac{E_i}{kT}\right\} \tag{4.4}$$

Where the integral form is the general definition ($\mathrm{d}\Gamma$ representing a trajectory in Hamiltonian phase space) and the latter is true for quantized systems, which our molecules are. g_i is the degeneracy of energy level E_i. The general form of the equation is important, because it lets us factor the partition function into parts that quantize differently. This happens by plugging in equation 4.6 in E, resulting in:

$$Q_{tot} = Q_e Q_v Q_r Q_t \tag{4.5a}$$

$$= \left[\sum_{i=0}^{\infty} g_i \exp\left\{-\frac{E_{ei}}{kT}\right\}\right] \times \left[\sum_{j=0}^{\infty} \exp\left\{-\frac{E_{vj}}{kT}\right\}\right] \times \left[\sum_{k=0}^{\infty} (2k+1) \exp\left\{-\frac{E_{rk}}{kT}\right\}\right] \times \left[\sum_{l=0}^{\infty} g_l \exp\left\{-\frac{E_{tl}}{kT}\right\}\right] \tag{4.5b}$$

As we see, electronic, rotational and translational energy levels have inherent degeneracy. The first is identical to the number of combinations arising from the spin multiplicity, whereas the latter two come from the combinatorics of one-dimensional motion contributions in three-dimensional space. Both equations 4.3 and 4.5 simplify a bit when one considers that we are using them to solve The Eyring Equation, in which the energy barrier $E_{TS} - E_R$ is specifically defined on a potential energy surface. Combining this fact with equation 4.3:

$$E_R - E_{TS} = E_{eR} + E_{ZR} - E_{eTS} + E_{ZTS} \tag{4.6}$$

E_Z here refers to the *zero-point energy*, the vibrational energy at zero temperature. The partition function simplifies as well, due to the fact that we are dividing Q_{TS} with Q_R. Translational energy is famously $E_t = \frac{1}{2}m\langle v^2\rangle$, which means that the translational partition functions cancel out, as neither mass nor temperature changes from R to TS. The electronic contributions to the partition function quotient cancel out (approximately) as well, as energy differences between molecular orbitals are high enough that only the ground state is occupied at room temperature, leaving $Q_{eR} \approx Q_{eTS} \approx g_i$. Naturally, this cancels out as well, since the transition state must have the same spin state as the reactant complex. This means that only the vibrational and rotational contributions are relevant for the statistical parameter in Equation 4.1:

$$\frac{Q_{TS}}{Q_R} = \frac{Q_{vTS}Q_{rTS}}{Q_{vR}Q_{rR}} \tag{4.7}$$

Now, let us derive all the functions in 4.9 and 4.10, in rising order of complexity. All energies are in principle solved by The Schrödinger equation:

$$\hat{H}\Psi = \hat{T}\Psi + \hat{V}\Psi = E\Psi \tag{4.8}$$

Rotational energy is separable into a molecule's three axes of rotation (A, B, and C), and it is governed by the equation:

$$E_r = \frac{\hat{T}(\Psi_{rA} + \Psi_{rB} + \Psi_{rC})}{\Psi_{rA} + \Psi_{rB} + \Psi_{rC}} = \frac{1}{2}\left(\frac{J_A^2}{I_A} + \frac{J_B^2}{I_B} + \frac{J_C^2}{I_C}\right) \tag{4.9}$$

Where J and I are the angular momentum and moment of inertia of each axis of rotation. The angular momenta are quantified by three rotational quantum numbers, the standard notation being J, K and L. This results in a rotational partition function,

as derived by [34].

$$Q_r = \sum_{J=0}^{\infty} \exp\left\{-\frac{J_A^2}{2I_A kT}\right\} \times \sum_{K=0}^{\infty} \exp\left\{-\frac{J_B^2}{2I_B kT}\right\} \times \sum_{L=0}^{\infty} \exp\left\{-\frac{J_C^2}{2I_C kT}\right\} \tag{4.10a}$$

$$= \frac{2\sqrt{2\pi}}{\sigma} \left(\frac{kT}{\hbar^2}\right)^{\frac{3}{2}} \frac{1}{\sqrt{I_A I_B I_C}} \tag{4.10b}$$

Where σ is a symmetry number, by default $\sigma = 1$ because all of our examined systems are all asymmetric rotors, that is, $I_A \neq I_B \neq I_C$. As we see, the difference between the reactant and transition state comes down to the moments of inertia changing as the nuclei move in relation to each other.

The vibrational energy of a (non-linear) molecule can be expressed as the sum of its' $3N - 6$ vibrational degrees of freedom, N being the number of nuclei. Each vibrational mode is characterized by a general coordinate q_u:

$$E_v = \sum_{u=1}^{3N-6} E_u(q_u) \tag{4.11}$$

These degrees of freedom were modelled using the harmonic oscillator approximation for simplicity. The harmonic model is roughly accurate for cases where the degree of freedom roughly corresponds to the stretching of a chemical bond, and where only a few levels of excitation are significantly populated at the relevant temperature. For larger molecules, some internal degrees of freedom are better described as internal rotations rather than vibrations, resulting in inaccuracies if their motion is described with a harmonic oscillator model [35]. This effect was neglected, as the resulting error was assumed to mostly cancel out upon division of Q_{TS} with Q_R.

$$-\frac{\hbar^2}{2\mu_u}\frac{\mathrm{d}^2\Psi_u}{\mathrm{d}q_u^2} + \frac{q_u^2}{2}\left(\frac{\mathrm{d}^2V}{\mathrm{d}q_u^2}\right)_0 \Psi_u = E_u\Psi_u \tag{4.12a}$$

$$E_u = \left(v_u + \frac{1}{2}\right)\hbar\nu_u \tag{4.12b}$$

Here μ_u is the effective mass of the vibrational motion, v_u is the vibrational quantum number and ν_u is the harmonic vibrational frequency. In Gaussian these are expressed in wavenumber units, which is obtained by dividing the equation below by $2\pi c$:

$$\nu_u = \sqrt{\frac{1}{\mu_u}\left(\frac{\mathrm{d}^2 V}{\mathrm{d}q_u^2}\right)_0} \tag{4.13}$$

Next, Q_v. As with Equation 4.8, the energy being a sum of $3N-6$ terms means the partition function is a product of $3N-6$ factors:

$$Q_v = \prod_{u=1}^{3N-6} Q_u = \prod_{u=1}^{3N-6} \sum_{v=0}^{\infty} \exp\left\{\frac{(v_u + \frac{1}{2})\hbar\nu_u}{kT}\right\} = \prod_{u=1}^{3N-6} \frac{1}{1-\exp\left\{-\frac{\hbar\nu_u}{kT}\right\}} \tag{4.14}$$

The vibrational frequencies are also solved using Frequency Analysis (see Chapter 4.1.3). One especially important detail is the fact that Q_{vTS} has $3N-7$ real vibrational modes and one imaginary, the imaginary mode corresponding the the reaction coordinate (This is easily seen from Equation 4.15, knowing that the coordinate has positive energy curvature). This is an important way of verifying that one has indeed found the Transition State during DFT calculations.

And most complex of all, the electronic energy E_e. For a molecule with N nuclei and M electrons, the electronic energy is governed by the following Schrödinger equation:

$$\hat{H}_e\Psi_e = -\frac{\hbar^2}{2m_e}\sum_{i=1}^{M}\nabla_i^2\Psi_e - \sum_{i=1}^{M}\sum_{j=0}^{N}\frac{Z_j e^2}{4\pi\epsilon r_{ij}}\Psi_e + \sum_{i=1}^{M}\sum_{k=1}^{M-i}\frac{e^2}{4\pi\epsilon r_{ik}}\Psi_e = E_e\Psi_e \tag{4.15}$$

Where Ψ_e is the electronic wavefunction. This is a very tricky equation, and our process of solving it will be fully detailed in chapters 4.1.4 through 4.1.6.

4.1.3 Frequency Analysis

The moments of inertia I_A, I_B, and I_C, as well as the $3N-6$ vibrational frequencies were calculated for optimized molecular structures (More on optimization later) using an approach entirely rooted in classical mechanics, which is sufficient, as the quantization of energy is already accounted for by equation 4.5. Moment of inertia calculations were initiated by determination of the centre of mass:

$$C_r = \frac{\sum_\alpha^N m_\alpha \vec{r}_\alpha}{\sum_\alpha^N m_\alpha} \tag{4.16}$$

after which the moment of inertia tensor is calculated:

$$I = \begin{vmatrix} I_{xx} & I_{yx} & I_{zx} \\ I_{xy} & I_{yy} & I_{zy} \\ I_{xz} & I_{yz} & I_{zz} \end{vmatrix} \qquad I_{ij} = \sum_\alpha^3 m_\alpha(\delta_{ij}\vec{r}_\alpha^2 - r_{\alpha,i}r_{\alpha,j}) \tag{4.17}$$

Here, I_A, I_B, and I_C are received by diagonalising the matrix [36].
For the vibrational frequencies, first a $3N \times 3N$ mass-weighted Hessian matrix is calculated in Cartesian coordinates:

$$f_{ij} = \frac{1}{\sqrt{m_i m_j}} \left(\frac{\partial^2 V}{\partial q_i \partial q_j} \right)_0 \tag{4.18}$$

Diagonalisation of this matrix gives $3N$ eigenvalues, of which 6 correspond to translational and rotational degrees of freedom, and the remaining $3N-6$ are the frequencies of the vibrational normal modes. This is then recalculated in $3N-6$ natural coordinates, directly corresponding to the normal modes. [36].

4.1.4 Solving the Electronic Wavefunction

In multi-particle quantum mechanics, multi-particle wavefunctions can be simplified by expressing it as a product of single-particle wavefunctions. The underlying assumption

here is that the wavefunction is separable even when accounting for inter-particle interactions. In quantum chemistry, a multi-electron wavefunction expressed as a product of single-particle wavefuntions is called a *Hartree product*:

$$\Psi_e = \prod_i^M \psi_i(r_i) \tag{4.19}$$

Complicating this picture is the fact that electrons have spin, meaning that single-electron wavefunctions must be antisymmetrical as required by the Pauli principle: $\Psi(r_i,...,r_j) = -\Psi(r_j,...,r_i)$. Hartree products do not satisfy this property, which is why the electronic wavefunction is usually expressed using *Slater Determinants*:

$$\Psi_e(r_1, r_2, ..., r_M) = \frac{1}{\sqrt{C!}} \begin{vmatrix} \psi_1(r_1) & \psi_2(r_1) & \dots & \psi_M(r_1) \\ \psi_1(r_2) & \psi_2(r_2) & \dots & \psi_M(r_2) \\ \vdots & \vdots & \ddots & \vdots \\ \psi_1(r_M) & \psi_2(r_M) & \dots & \psi_M(r_M) \end{vmatrix} \tag{4.20}$$

where C is a normalisation constant, and each ψ_i is a spin orbital contributing to the molecular orbitals. The Slater Determinant is the most efficient way to describe an electronic wavefunction consisting of antisymmetrical spin orbitals. Plugging this into equation 4.15 to solve the Schrödinger Equation is a computational approach called the *Hartree-Fock Equation* (HF). The weakness of this approach is that as that it is only able to account for the interactions between spin orbitals on average. Among other effects, this leaves out the extent to which electrons in neighbouring orbitals influence the shape of an orbital with Coulomb repulsion. The error caused by this inaccuracy is small compared to the total electronic energy of the molecule (on the order of 1%), but very significant if one is trying to calculate subtle differences in energy along a potential energy surface, as we are. Electronic effects not accounted for by this method are called *electron correlation*, And these are addressed in quantum chemical computations by linear combination of several Slater determinants [37]. Attempts to calculate accurate electronic energies thus typically consist of a HF calculation followed by electron

correlation methods.

One way to summarize all we've learned so far is that equation 4.15 is a very complicated equation indeed, and that it is analytically unsolvable, due to consisting of $M + N$ interacting particles. Numerical iterative methods must be used. The usual approach in computational chemistry is to express the atomic spin orbitals using *basis sets* composed of *basis functions*, essentially roughly orbital-shaped gaussian trial functions. The molecular orbitals are expressed as linear combinations of a suitable amount of basis functions μ [38],[37].

$$\psi_i \approx \sum_{\mu} c_{\mu i} \mu \tag{4.21}$$

The larger the amount of basis functions, the more accurately the end result is likely to represent the real wavefunction. Naturally, this also comes with an increased computational cost.

Two basis sets were used in molecular structure optimization calculations to manage this trade-off between computational cost and accuracy (A third was used for Coupled-Cluster calculations, see Chapter 4.1.5). The simpler basis set used for lower 'level of theory' calculations was the 6-31+G*. This is a Double-Zeta Split-Valence type basis set, meaning that valence electrons are expressed using two separate basis functions. The notation means that each atomic orbital is expressed using 6 primitive gaussian functions, and that the two basis functions used for the valence orbitals are composed of 3 and 1 basis functions, respectively. The asterisk means that polarisation functions are calculated for all heavy atoms to help describe their polar bonds, particularly with hydrogen atoms [39]. The + means that diffuse supplementary functions are calculated for all non-hydrogen atoms [40]. These diffuse functions are supplementary orbitals describing the 'tail-ends' of molecular orbitals, in situations where electron

density far from the nuclei is non-negligible.

Aug-cc-pVTZ was the basis set used for higher level of theory calculations. Here cc stands for 'correlation-consistent', meaning that the set's main use is to perform electron-correlation corrections. The valence orbitals as expressed here using three basis functions (VTZ stands for Valence Triple-Zeta). p means that polarization functions are calculated, and Aug means that diffuse functions are added, for the same purpose as in the 6-31+G* basis set [41]. Unlike 6-31+G* however, the Aug-cc-pVTZ basis set includes multiple polarization and diffuse functions for all atoms in the system.

Now, as we have covered some of the main tools that make up a generic rate calculations, let us go further into the specifics of the procedure. As we covered in Chapter 4.1.2, the vibrational and rotational energies of a molecule are fairly easy to calculate, whereas electronic energies are very difficult. However, to accurately determine the vibrational frequencies and moments of inertia as covered in Chapter 4.1.3, we have to know the equilibrium 3D structure of the molecule, which naturally depends on the electronic interactions. This means that the electronic structure of the molecule must be determined before the frequency analysis. As we have seen in this chapter, determining the precise electronic energy is quite a complex process, and as such the following procedure is followed for the calculations concerning each chemical structure (Reactant, product, or transition state):

1. Efficient optimization of the equilibrium molecular structure

2. Calculation of vibrational frequencies and moments of inertia

3. Determination of the exact electronic energy

The Frequency Analysis we have already covered. The determination of the electronic energy was implemented using Couple-Cluster calculations, which is covered in Chapter

4.1.5, and the optimization was implemented using density functional theory, which is covered in Chapter 4.1.6.

4.1.5 Coupled-Cluster Theory

The essential idea behind Coupled-Cluster Theory is solving the Schrödinger Equation by using an exponential ansatz of the kinetic energy to 'probe' the ground state wave-function, thereby giving us accurate information on its structure and energy. It is a much more accurate computational approach than DFT when it comes to calculating the energy, but also considerably more expensive, which is why the optimization of the structure is done using DFT. The exponential ansatz has the following form:

$$\Psi_{CC} = \exp\Big\{\hat{T}\Big\}\Psi_0 = \left[1 + \hat{T} + \frac{\hat{T}^2}{2!} + \frac{\hat{T}^3}{3!} + ...\right]\Psi_0 \tag{4.22}$$

Inserting the exponential ansatz into the Schrödinger equation and applying the reverse operation allows us to solve for the energy:

$$\exp\Big\{-\hat{T}\Big\}\hat{H}\exp\Big\{\hat{T}\Big\}\Psi_0 = \exp\Big\{-\hat{T}\Big\}E\exp\Big\{\hat{T}\Big\}\Psi_0 = E\Psi_0 \tag{4.23}$$

This approach gets very expensive because the kinetic operator is expressed as a sum of multiple levels of excitation, $\hat{T} = \hat{T}_1 + \hat{T}_2 + \hat{T}_3 + ...$, where each individual $\hat{T}_n$ operator excites n electrons to higher orbitals. [38] This detail is important for the terminology of Coupled-cluster theory, since levels of theory and detail are named after these. Coupled-cluster singles (CCS) calculations account for $\hat{T}_1$, in the exponential ansatz, coupled-cluster doubles (CCD) account for $\hat{T}_2$, whereas Coupled-cluster singles, doubles & (triples) (CCSD(T)), the level of theory used in our calculation, accounts for $\hat{T}_1 + \hat{T}_2$ using the normal approach and adds triply excited states on top using perturbation theory, a common method for quantifying small deviations from known systems in Quantum Physics. We will not describe it in full detail here, as it is readily described in the literature. [38] The significance of this approach in our case is that

it effectively splits of the calculation into two parts, $E = E_{CCSD} + E_T$, in which the computational cost of the CCSD part scales with system size by N^6, whereas the perturbative part scales by N^7. The former is more mathematically complex, which means that CCSD(T) calculations are much more economical than full CCSDT calculations for larger molecules.

The basis set used for the Coupled-cluster calculations was cc-pVDZ-F12, a valence double-zeta basis set where F12 means that the base Slater Determinant is complemented with *geminal* determinants accounting for the impact of adjacent electrons to each orbital as a function of electronic distance r_{12} [42]. F12 here refers to $f_{12}(r_{12})$, as opposed to R12-methods, where the correlation effects are simply scaled by r_{12}^{-1}. This approach is not fully necessary for accounting for the electron correlation, but it does accelerate the convergence of the Coupled-Cluster calcultions.

4.1.6 Density Functional Theory

As alluded to previously, Density Functional Theory was the chosen method to optimize the structure of the molecules for energy calculations. The method is well suited to this purpose, because its entire premise is to mostly bypass the wavefunctions and express the electronic interactions using a different formalism.

The theoretical framework of density functional theory is based on the Kohn-Sham and Hohenberg-Kohn Theorems, showing that Equation 4.15 is analytically solvable for the electronic ground state in the special case where we have accurate knowledge of the electron density $\rho(r)$ [43]. Naturally, due to the analytical unsolvability of the multi-particle Schrödinger Equation, we do not have accurate knowledge of the electron density, but the implication is that we can optimise the structure of the molecule by minimizing the energy as a function of ρ. This means that the $3M$-

dimensional problem of the electronic structure is effectively reduced to a 3-dimensional problem. The density is formally defined as the total electronic probability density:

$$\rho = \sum_{i=1}^{M} \Psi_i^* \Psi_i \tag{4.24}$$

Next, let's look at how the electronic energy expression changes when expressed in terms of the electron density:

$$E(\rho) = T(\rho) + V_{eN}(\rho) + V_{ee}(\rho) + E_{xc}(\rho) \tag{4.25}$$

Here T is the kinetic energy, whereas V_{eN} and V_{ee} are the potential energy contributions of electron-nucleus and electron-electron Coulomb interactions, respectively. These terms are all analytically solvable. E_{xc}, however, is the *exchange-correlation* energy, combing together the energy contribution of all effects difficult to quantify in the ρ-formalism. Electron correlation we are already familiar with, but the *exchange interaction* we have only covered using different terminology. It is the energy arising from the antisymmetry of wavefunctions as imposed by the Pauli Principle. Spin orbitals wavefunctions have this as an inherent mathematical property, but the electron density doesn't, which means that its effects have to be parametrized using trial *density functionals* when optimizing the molecular structure as a function of ρ.

Density functionals are categorized according to 'levels of theory', an often used shorthand for the complexity and accuracy of the functional, going from *local density approximation* (explicitly calculating the exchange-correlation for a uniform electron cloud) to full explicit calculation of both the exchange interaction and the electron correlation. The full scale of these is presented in a well known visual metaphor in *Jacob's ladder*, where LDA is on rung one and the full explicit calculation is on rung five [44]. The two functionals used in this work, B3LYP and ωB97XD, both belong to rung four of the ladder. Both of these are hybrid functionals, combining multiple

simpler approximations for both the exchange and correlation and parametrizing them. We will leave a full description of the ingredients to the original sources, but in short, B3LYP combines the LDA approximation with a generalized gradient approximation ($\nabla\rho$ is parametrized separately to ρ) and the Hartree-Fock energy calculated from a two-electron density-matrix [45],[46],[47]. ωB97XD on the other hand calculated the electron correlation by combining long-range and short-range Slater Determinants [48] with a more complex generalized gradient model [49], and an empirical atomic pair-by-pair dispersion interaction correction [50].

Of the two density functional used, B3LYP is simpler and thus computationally cheaper, and was thus used for initial optimization. The higher level of theory ωB97XD functional was used to adjust the final touches to the molecular geometry.

4.2 The Structure-Activity Relationship

Structure-Activity Relationships (SAR) are a quick, easy, and user-friendly computational tool for quick estimation of the order of magnitude for a reaction rate. Its main assumptions are:

1. A molecule is a sum of its parts.
2. Only functionalities close to the reactive center matter for the reaction rate.

Naturally, this does not make for a very good descriptive model of real chemical interaction. Most notably, it neglects the intramolecular electrodynamic interactions between the functional groups (these matter both close to and far away from the reactive center!), as well as steric effects constricting the 3D structure of the molecule. Related to both of these points, the length and shape of the carbon chain are mostly unaccounted for. Nevertheless, SAR-models are useful because they boil down complex chemical interactions to very simple equations whose results are rarely more than two

orders of magnitude off. They therefore are a very starting point for quickly estimating which reactions occur and which don't, and which reactions are worth doing more precise quantum chemical calculations on.

In our case, the SAR we are mainly using is Veerecken's & Peeters's alkoxy bond scission SAR, based on a large body of quantum chemical calculations, primarily at the B3LYP/6-31G level of theory. In the model, bond scission rates are estimated by simplifying the Eyring Equation to an Arrhenius-like expression:

$$k_S = L \cdot A_{SAR} \exp\left\{\frac{-E_{SAR}}{kT}\right\} \tag{4.26}$$

Where L is the reaction path degeneracy (By default $L = 1$, unless the alkoxy radical has multiple identical β-carbons.), and $A_{SAR} = \frac{kT}{h}\frac{Q_{TS}}{Q_R}$, which is assumed to equal $A_{SAR} = 1{,}8 \cdot 10^{13}\ \mathrm{s}^{-1}$ at room temperature for all alkoxy radicals based on work by Peeters [51]. This is naturally where the neglect of steric effects comes in, as those are accounted for in the Eyring Equation by the partition functions. As a molecule is assumed to be a sum of its parts, the activation barrier E_{SAR} is expressed as a linear sum of energy contributions from each of the functionalities attached to either the α-carbon or the β-carbon. Its equation is:

$$E_{SAR} = E_{SAR}(\mathrm{C_2H_5O}\cdot) + \sum_s F_s \cdot n(s) \tag{4.27}$$

$E_{SAR}(\mathrm{C_2H_5O}\cdot) = 74{,}9\frac{\mathrm{kJ}}{\mathrm{mol}}$ being the energy barrier for the simplest possible alkoxy radical capable of undergoing the scission reaction, F_s being the energy contribution from substituent s, and $n(s)$ being the number of s-substituents. This equation resulted in acceptably accurate results at $E_{SAR} > 29{,}3\frac{\mathrm{kJ}}{\mathrm{mol}}$, but poor results below. In

those cases, Vereecken & Peeters suggest the following exponential parametrisation:

$$E'_{SAR} = A \exp\left\{\frac{-(E_{SAR} - B)^2}{C}\right\} = 79{,}5\frac{\text{kJ}}{\text{mol}} \exp\left\{\frac{-(E_{SAR} - 92{,}05\frac{\text{kJ}}{\text{mol}})^2}{941{,}4(\frac{\text{kJ}}{\text{mol}})^2}\right\} \quad (4.28)$$

Since part of the point of the research was combining calculations and experiments, an important criteria for the systems chosen for research was experimental viability (in addition to atmospheric relevance, obviously). As such, the 112 aliphatic alkenes with 3-8 carbon atoms commercially available at Sigma-Aldrich. O_3, $OH\cdot$, and $NO_3\cdot$-oxidation products were drawn for all of these. For O_3-oxidation, special attention drawn to which of the Criegee Intermediates formed (See Figure 2.4) have rapid H-shift reactions and which don't. [11] Examples of the drawn mechanisms for a few specific molecules can be found in Chapter 5.1. For $OH\cdot$ oxidation, Atkinson's SAR (the relevant values of which were introduced in Chapter 1.2) on $OH\cdot$ reactivity was implemented to determinate which peroxy radicals, and consequently which alkoxy radicals, are formed. For $NO_3\cdot$, as has been established, the same reactivity rules apply with even stronger differences in rates. As such, the same alkoxy radical intermediates were assumed with the β-OH simply replaced by a β-ONO_2 as per Figures 1.1 and 1.3.

Table 4.1: Exact energy contributions of the substituents relevant to Tables 4.2-4.4. [32] The energies are expressed in $\frac{\text{kJ}}{\text{mol}}$ ($\frac{\text{kcal}}{\text{mol}}$ in the original source).

Substituent	F_s
α-alkyl	-9,6232
α-C=O	-2,9288
α-C=C	-20,5016
α-OH	-37,2376
α-NO_2	-9,2048
α-c-butyl	-8,368
β=O	-35,564
β-alkyl	-14,2256
β-C=C	-40,1664
β-OH	-31,38
β-ONO_2	-11,7152
β-c-pentyl	-29,288
4-ring opening	-71,5464
5-ring opening	-36,4008
6-ring opening	-26,3592

SAR calculations were implemented on all distinguishable alkoxy radicals formed in the mechanisms. The energy contributions of the relevant substituents, summarized from source, are presented in Table 4.1. Results of the SAR calculations are presented in Tables 4.2, 4.3, and 4.4 for ozonolysis, $OH\cdot$-oxidation and $NO_3\cdot$-oxidation, respectively.

A quick comparison of the values for β=O and α-C=O in Table 4.1 already tells us a fundamental fact about the alkoxy radicals formed from ozonolysis: The carbonyl

formed from in the decomposition of the VHP (See Figure 2.4) is almost always the β-carbon. This is due to the stabilizing effect the C=O-bond has on the formed $R' \cdot$-radical. As we see from Table 4.2, however, there are a couple of systems where the right combination of functional groups in what would otherwise have been an 'α-alkyl'-substituent enables a scission reaction competitive with the β-oxo scission.

Next, oxidation by $OH \cdot$. As with the ozonolysis-derived alkoxy radicals, we see that carbon attacked by the $OH \cdot$ is by far the most likely candidate for β-carbon due to the significant negative energy contribution of the OH group. If an adjacent bond has a competitive scission reaction, is most likely is due to another OH group the alkene already had before the oxidation reaction. These are somewhat slower than the scission rates for ozonolysis-derived alkoxy radicals. Since we have no prior knowledge of the Intersystem Crossing rates for these systems, one might therefore assume that the scission pathway of $OH \cdot$-derived alkoxy radicals is of equal atmospheric significance as for O_3-derived ones.

As established in Chapter 1.2, $NO_3 \cdot$ oxidation occurs quite similiarly to $OH \cdot$ oxidation, expect that we get a nitro substituent instead of a hydroxy one. As such, Table 4.4 differs from Table 4.3 only in energies.

Table 4.2: Approximate SAR results for all of the relevant Ozonolysis-derived alkoxy bond scissions reactions. Energies are presented in $\frac{\text{kJ}}{\text{mol}}$. Note: 'n-ring' means here that both the α- and β-carbons are part of a ring of that size, and that the bond scission consequently opens the ring.

α-substituent	β-substituent	$\sum_s F_s \cdot n(s)$	E_{SAR}	E'_{SAR}	k_S
	C=O	-35,56	39,33	39,33	2,30E+06
	C=O, alkyl	-49,79	25,10	25,52	6,15E+08
alkyl	C=O	-45,19	29,71	29,71	1,12E+08
alkyl	C=O, alkyl	-59,41	15,48	17,99	1,29E+10
	C=O, C=C	-75,73	-0,84	8,79	4,97E+11
alkyl	C=O, C=C	-85,35	-10,46	5,44	1,94E+12
C=C	C=O	-56,07	18,83	20,50	4,82E+09
C=C	C=O, alkyl	-70,29	4,60	11,30	1,80E+11
C=C, alkyl	C=O	-65,69	9,20	13,81	6,54E+10
C=C, alkyl	C=O, alkyl	-79,91	-5,02	7,11	9,58E+11
	C=O, c-pentyl	-64,85	10,04	14,23	5,35E+10
4-ring	C=O	-107,11	-32,22	1,67	9,53E+12
6-ring	C=O	-61,92	12,97	16,32	2,55E+10
OH	C=O	-72,80	2,09	10,04	2,95E+11
C−C=O	OH	-34,31	40,58	40,58	1,38E+06
C−C=O	OH, alkyl	-48,53	26,36	26,78	3,94E+08
C−C=O	OH, C=C	-74,48	0,42	9,62	4,00E+11

Table 4.3: SAR results for all of the relevant OH·-oxidation derived alkoxy bond scissions reactions. Energies are presented in $\frac{\frac{kJ}{mol}}{mol}$.

α-substituent	β-substituent	$\sum_s F_s \cdot n(s)$	E_{SAR}	E'_{SAR}	k_S
	OH	-31,4	43,5	43,5	4,24E+05
alkyl	OH	-41,0	33,9	33,9	2,06E+07
2 x alkyl	OH	-50,6	24,3	24,7	8,22E+08
	OH, alkyl	-45,6	29,3	29,3	1,32E+08
alkyl	OH, alkyl	-55,2	19,7	20,9	3,72E+09
2 x alkyl	OH, 2 x alkyl	-84,9	-10,0	5,4	1,85E+12
c-but	OH	-45,6	29,3	29,3	1,32E+08
c-hex	OH	-39,8	35,1	35,1	1,24E+07
5-ring	OH	-67,8	7,1	12,6	1,06E+11
6-ring	OH	-57,7	17,2	19,2	7,95E+09
6-ring, NO_2	OH	-66,9	7,9	13,4	8,74E+10
C=C	OH	-51,9	23,0	23,8	1,26E+09
C=C, alkyl	OH	-67,4	7,5	13,0	9,61E+10
C=C, alkyl	OH, alkyl	-75,7	-0,8	8,8	4,97E+11
	OH, C=C	-71,5	3,3	10,9	2,32E+11
	OH, C=C, alkyl	-85,8	-10,9	5,4	2,04E+12
alkyl	OH, C=C	-81,2	-6,3	6,7	1,14E+12
2 x alkyl	OH, C=C	-90,8	-15,9	4,2	3,40E+12

Table 4.4: SAR results for all of the relevant $NO_3\cdot$-oxidation derived alkoxy bond scissions reactions. Energies are presented in $\frac{\text{kcal}}{\text{mol}}$.

α-substituent	β-substituent	$\sum_s F_s \cdot n(s)$	E_{SAR}	E'_{SAR}	k_S
	ONO_2	-11,7	63,2	64,4	1,52E+02
alkyl	ONO_2	-21,3	53,6	54,4	7,37E+03
2 x alkyl	ONO_2	-31,0	43,9	44,4	3,58E+05
	ONO_2, alkyl	-25,9	49,0	49,8	4,72E+04
alkyl	ONO_2, alkyl	-35,6	39,3	39,3	2,30E+06
2 x alkyl	ONO_2 , 2 x alkyl	-59,4	15,5	18,0	1,29E+10
c-but	ONO_2	-20,1	54,8	56,1	4,44E+03
c-hex	ONO_2	-20,1	54,8	56,1	4,44E+03
5-ring	ONO_2	-43,1	31,8	31,8	4,80E+07
6-ring	ONO_2	-43,1	31,8	31,8	4,80E+07
6-ring, NO_2	ONO_2	-47,3	27,6	27,6	2,50E+08
C=C	ONO_2	-32,2	42,7	42,7	5,95E+05
C=C, alkyl	ONO_2	-41,8	33,1	33,1	2,89E+07
C=C, alkyl	ONO_2, alkyl	-56,1	18,8	20,5	4,82E+09
	ONO_2, C=C	-43,1	31,8	31,8	4,80E+07
	ONO_2, C=C, alkyl	-57,3	17,6	19,2	7,03E+09
alkyl	ONO_2, C=C	-61,5	13,4	16,3	2,28E+10
2 x alkyl	ONO_2, C=C	-71,1	3,8	10,9	2,13E+11

As we see, the peroxy radicals formed by $NO_3\cdot$-oxidation have relatively slow bond scissions, meaning that the bond scission pathway is unlikely to be dominating for these systems, unless the alkene in question has a scission rate enchanting β-functionality (such as an OH group) next to the C=C-double bond. In the few cases where the β-ONO_2-scission is competitive, Vereecken & Peeters make the foot-

note that the product radicals decompose further, forming a carbonyl and a nitrogen dioxide radical:

$$\mathrm{RCONO_2CO \cdot R} \longrightarrow \mathrm{RC \cdot ONO_2 + COR} \longrightarrow \mathrm{2COR + NO_2 \cdot} \tag{4.29}$$

In other words, $NO_3 \cdot$-oxidation derived peroxy radicals are unlikely to form ROR′ dimers, and in the case that they do, they are a result of a different bond scission as in the $OH \cdot$ oxidation. Figure 4.1 illustrates what is meant by this:

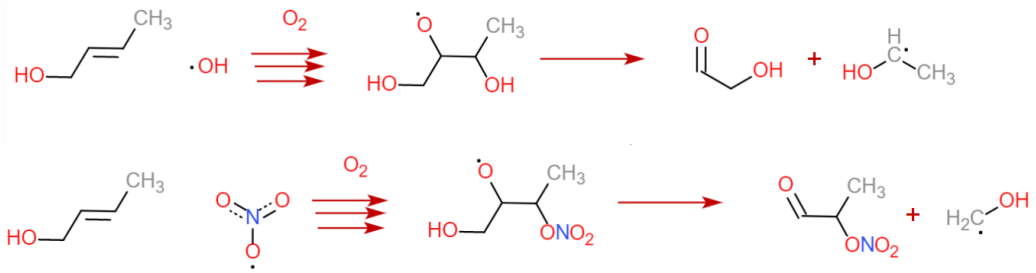

Figure 4.1: A simplified schematic illustrating the difference in bond scission route takes by $OH \cdot$ and $NO_3 \cdot$-derived alkoxy radicals from the same precursor alkene. The shown alkoxy radical is only one of two (equally likely according to Atkinson's SAR, but the interaction between the OH group and the reactant may shift the balance one way or another), chosen to demonstrate the fact the competition between the two bond scission mechanisms. In the $OH \cdot$ case, the shown scission reaction dominates with two orders of magnitude whereas in the $NO_3 \cdot$ case, it dominates by one order.

4.3 Quantum Chemical Calculations

The systems chosen for Quantum chemical calculations were based on the results of Tables 4.2-4.4, with special emphasis placed on our ability to do experiments on the same systems. As we will see in Chapter 5.2, Ozonolysis is by far the easiest of the three oxidation reactions to measure experimentally. This is fortunate, as the SAR results show that Ozonolysis-derived alkoxy bond scissions are somewhat more likely to be atmospherically relevant than OH-oxidation derived alkoxy bond scissions, and a great

deal more atmospherically relevant than $NO_3\cdot$-oxidation derived alkoxy bond scissions.

The main focus of the QC calculations was placed on modelling two effects left unaccounted for by Vereecken's & Peeters's SAR. Firstly, variation of carbon chain length in Ozonolysis-derived alkoxy radicals such as those seen in Figure 2.4, as this was thought to add a good complement to already existing models, and secondly, the impact of amine groups on alkoxy bond scission in both O_3 and $OH\cdot$-derived alkoxy radicals, as these were missing completely from the SAR.

The following procedure of Gaussian calculations was followed for the calculation of each bond scission rate: First, the commercial Spartan program was used to calculate the conformer distribution for each reactant molecule under investigation. B3LYP/6-31+G* runs were implemented on all conformers, and the conformers with energy considerably higher than the minimum were filtered out. This was followed by a ωB97XD/6-31+G* -run. Again, the highest energy conformers were filtered out, and final adjustments to the structure were done with ωB97XD/aug-cc-pVDZ, with Frequency analysis implemented on the resulting structure. After this, a CCSD(T)-F12/VDZ-F12 run was done on the lowest energy conformer. For the transition state, the resulting structure of the ωB97XD/aug-cc-pVDZ-run was opened in Spartan, in which the scissioning bond was streched a suitable amount. A constricted conformer distribution was implemented with the relevant bond length held constant. Each resulting conformer was subject to a constrained B3LYP/6-31+G* optimisation, followed by a B3LYP/6-31+G* -level Transition State (energy saddle point) search followed by Frequency Analysis to make sure that the imaginary vibrational mode was found, and that corresponded to a stretching motion of the scissioning bond. In this case, the found transition state was optimised with a ωB97XD/aug-cc-pVDZ, again followed by Frequency Analysis and CCSD(T)-F12/VDZ-F12 -calculation of the electronic energy.

As both the reactants and the transition states were radicals, all calculations were implemented as spin-unrestricted with a doublet as the presumed state. Some of the final ωB97XD/aug-cc-pVDZ-calculations were implemented in Gaussian with the 'Loose' -option on, meaning that a looser numerical criteria was used when looking for the energy saddle point. This is a potential source of error.

Products were neglected apart from energy optimisation of CH_2O and $CHO\cdot$ resulting from the bond scission of the simplest possible ozonolysis-derived alkoxy radical. This is because products are needed for two reasons: Calculating the tunnelling factor κ, which we know will be insignificant, and for evaluating the thermochemistry of the reaction. The first was neglected for reasons detailed in Chapter 4.1.1, and the latter was neglected due to a simple observable trend of the scission reactions. First, they always form two product molecules from one reactant molecule, increasing the entropy of the system. Secondly, they all form a stable C=O bond from a weak C−O bond, meaning they are highly likely to be exothermic. According the the second law of thermodynamics for constant p and T, chemical reactions with $\Delta S > 0$ and $\Delta H < 0$ are spontaneous under all conditions:

$$0 \geq \Delta G = \Delta H - T\Delta S \tag{4.30}$$

4.4 Results and Discussion

The results of the chain variation calculations are summed up in Table 4.5, grouped by substituents. The results show that the barrier energies are generally lower that those predicted by the SAR. In addition, we see that increasing the length of the carbon chain further decreased the barrier energy, and that the length of the β-chain has a larger impact than the length of the α-chain. This is to be expected, as the length of the β-chain has a direct impact on the stability of the formed $R'\cdot$-radical. The

partition functions were higher for the Transition State than for the Reactant, which is also to be expected, as these are dissociation reactions. The two exceptions are most likely related to specific geometric properties of the global minimum conformers and transition states.

Table 4.5: Calculated bond scission rates for ozonolysis-derived alkyl-substituted alkoxy radicals.

Subst.	Subst.	E ($\frac{\text{kJ}}{\text{mol}}$)	E ($\frac{\text{kJ}}{\text{mol}}$)	$\frac{Q_{TS}}{Q_R}$	$k \sim$ s^{-1}	$k \sim$ s^{-1}
α	β	ωB97	F12	ωB97	ωB97	F12
H	H	36,68	31,53	7,863	1,81E+07	1,45E+08
H	Met	23,70	16,11	6,160	2,69E+09	5,74E+10
H	Et	23,23	15,26	5,629	2,96E+09	7,38E+10
H	Prop	22,53	14,47	6,516	4,54E+09	1,18E+11
Met	H	27,39	21,12	2,434	2,39E+08	3,00E+09
Met	Met	16,45	11,09	3,768	3,06E+10	2,67E+11
Met	Et	15,94	10,56	3,668	3,66E+10	3,21E+11
Met	Prop	16,22	11,38	0,969	8,64E+09	6,08E+10
Et	H	26,65	20,72	2,255	2,99E+08	3,27E+09
Et	Met	14,52	8,64	3,750	6,63E+10	7,13E+11
Et	Et	13,99	8,07	3,562	7,82E+10	8,53E+11
Et	Prop	9,26	4,34	0,630	9,33E+10	6,80E+11
Prop	H	26,93	21,00	3,341	3,95E+08	4,33E+09
Prop	Met	14,82	8,93	3,355	5,26E+10	5,66E+11
Prop	Et	11,26	5,18	4,173	2,76E+11	3,21E+12
Prop	Prop	13,92	5,95	4,113	9,29E+10	2,32E+12

An attempt was made to fit the barrier energies to a function, as they were observed to have a roughly exponential relation to the chain length. The most successful fit was a 2D plane fit of $\ln E$ as a function of the number of carbon atoms in both

substituents. The results was $R^2 \approx 0{,}77$, due to the existence of several outliers. One might therefore say that the barrier energy only has a roughly exponential relation to the carbon chain length. The fit might have succeeded better if butyl substituents had been considered as well, but this was considered an non-optimal use of computational resources. For the record, the 2D fit resulted in the function:

$$\Delta E = (28{,}41309 \pm 4{,}33130)\frac{\text{kJ}}{\text{mol}} \exp\{(-0{,}26009 \pm 0{,}0635)\alpha\} \exp\{(-0{,}3346 \pm 0{,}06357)\beta\}$$

where α and β are the number of carbons in the α and β-substituents, respectively.

Next, a series of quantum chemical computations was implemented on the impact of amines of ozonolysis-derived alkoxy radicals. The results are summarised in Table 4.6. The results show that scission reactions where the closed-shell product is an amide have submerged barriers. This fact makes perfect chemical sense, as for these reactions both the radical product and the closed-shell product are resonance-stabilized, meaning that the transition state must have an even higher degree of conjugation. This would explain why it is lower in energy compared to the reactant molecule.

During the saddle point search of the alkoxy radicals with $\alpha - \text{CH}_2\text{NH}_2$ and $\alpha - \text{CH}_2\text{NHMet}$, the molecule occasionally drifted into an uncharted region of configuration space, one in which the $\text{CH}_2\text{NH}_2\cdot$ radical had dissociated from the rest of the molecule, leaving a dicarbonyl as the second product. This was taken as a suggestion that there exists a competing bond scission reaction. A new series of reaction rates was promptly calculated to compare these two reactions.

Table 4.6: Calculated bond scission rates for ozonolysis-derived amine-including alkoxy radicals. For negative barrier energies, the reactions rates are calculated using $k = \frac{kT}{h}\frac{Q_{TS}}{Q_R}$ only.

Subst.	Subst.	E ($\frac{\text{kJ}}{\text{mol}}$)	E ($\frac{\text{kJ}}{\text{mol}}$)	$\frac{Q_{TS}}{Q_R}$	k s^{-1}	k s^{-1}
α	β	ωB97	F12	ωB97	ωB97	F12
NH_2	H, C=O	-21,27	-11,18	0,893	5,55E+12	5,55E+12
NHMet	H, C=O	1,72	-7,32	1,895	5,88E+12	1,18E+13
CH_2NH_2	H, C=O	34,34	30,18	2,559	1,52E+07	1,92E+09
CH_2NHMet	H, C=O	33,83	26,65	2,094	1,53E+07	6,35E+09
H	NH_2, C=O	34,31	36,14	2,653	1,59E+07	5,74E+07
H	NHMet, C=O	33,98	34,32	17,919	1,23E+08	5,58E+08
H	CH_2NH_2, C=O	24,09	17,92	4,638	1,73E+09	3,16E+11
H	CH_2NHMet, C=O	25,12	16,94	5,580	1,37E+09	6,06E+11

Table 4.7: Rates of alkoxy bond scission for amine-including alkoxy radicals. Notation same as above.

Subst.	Subst.	E ($\frac{\text{kJ}}{\text{mol}}$)	E ($\frac{\text{kJ}}{\text{mol}}$)	$\frac{Q_{TS}}{Q_R}$	k s^{-1}	k s^{-1}
α	β	ωB97	F12	ωB97	ωB97	F12
CH_2NH_2	H, C=O	34,34	22,35	2,559	1,52E+07	1,92E+09
CH_2NHMet	H, C=O	33,83	18,89	2,094	1,53E+07	6,35E+09
CH_2NH_2	H, OH	35,41	28,51	2,847	1,71E+07	6,16E+07
CH_2NHMet	H, OH	34,09	22,99	1,215	8,36E+06	3,79E+07

Now, to sum up what we have learned, there do seem to exist a large variety of atmospheric oxidation-derived peroxy radicals, for which the alkoxy bond scission is fast enough to compete with the other pathways. Particularly the peroxy radicals formed in ozonolysis, and to a lesser extent OH$\cdot$-oxidation, have very rapid bond

Table 4.8: Reaction rates of the competing bond scission pathway, resulting in a $CH_2NH_2\cdot$-radical and a carbonyl.

Subst.	Subst.	E ($\frac{kJ}{mol}$)	E ($\frac{kJ}{mol}$)	$\frac{Q_{TS}}{Q_R}$	k s^{-1}	k s^{-1}
α	β	ωB97	F12	ωB97	ωB97	F12
CH_2NH_2	H	11,52	12,70	1,748	8,20E+11	2,14E+12
CH_2NHMet	H	6,40	4,02	1,552	2,26E+12	4,92E+12
CH_2NH_2	H, C=O	3,59	1,67	1,062	7,39E+12	7,64E+13
CH_2NHMet	H, C=O	-0,28	-6,07	0,910	5,65E+12	5,65E+12
CH_2NH_2	H, OH	4,48	-0,76	1,466	5,66E+06	9,11E+12
CH_2NHMet	H, OH	6,22	-3,24	5,019	2,53E+12	3,12E+13

scission reactions.

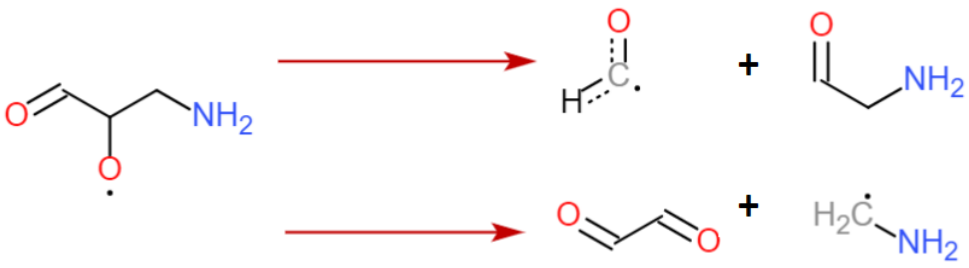

Figure 4.2: The two competing scission reactions for alkoxy radicals with an amine group in the γ-position: The alkoxy bond scission and the dicarbonyl forming scission.

5. Experimental Studies

Now that we have calculated a large number of bond scissions rates, we can attempt to use this information to start looking for ROR′ formation experimentally. The experiments were done by directly oxidizing commercially available alkenes and measuring the products using time-resolved NO_3^--Chemical Ionization Atmospheric Pressure interface Time-of-flight Mass Spectrometry (NO_3^--CIMS-APi-TOF). Two alkene precursors were present in the chamber during measurements: The precursor of the radical whose reactions we want to measure, and cyclohexene as a reactant partner to improve detectability. $OH\cdot$ formed from the dissociation of vinylhydroperoxide (See Figure 2.4) was removed using CO as a scavanger. The full details of the experimental setup are covered in Chapter 5.2.

5.1 Alkenes Chosen for Experiments

The choice of alkene reactants was based on a couple of simple criteria: First, the ozonolysis reaction had to be simple enough so as to not produce more than two unique peroxy radicals. This was to simplify the quantification of dimers from the mass spectra (The main factor limiting this is the amount of of formed unique Criegee Intermediates with rapid H-shifts). Second, molecules with very rapid scission rates were preferred, to decrease the possibility that possibly formed ROR' dimers would have concentrations below the limit of quantification. Third, relatively cheap reactants were preferred to expensive reactants, for fairly obvious reasons. Based on these

criteria, three componds were chosed: 2,3-Dimethyl-2-butene (Tetramethylethylene, or TME), 2-Metyl-2-propen-1-ol (Isobutenol), and 2-Metyl-2-propen-1-amin (Isobutenamine). Ozonolysis mechanisms are presented in Figures 5.1, 5.2, and 5.3.

A short note on the reaction mechanism notation used in the figures: As shown in Figure 2.4, the first stage of the ozonolysis reaction can form two kinds of Criegee Intermediate conformers, here referred to as *syn* and *anti*. In addition to this, the carbonyl oxide functionality can end up on either side of the alkene double bond, whereas the other side gets a carbonyl. This means that there is a total of four different Criegee Intermediates that might form from the ozonolysis of a generic alkene, all of which may or may not have the unimolecular H-shift as their main sink reaction. As such, all four possible CI:s are presented in the figures, even if some are chemically identical. The formed carbonyls are not shown, because they do not partake in the formation of peroxy radicals.

Since the ozonolysis reaction is an active source of $OH\cdot$ radicals, and since $OH\cdot$ oxidation of alkenes is considerably faster than ozonolysis, the reaction forms a competitive oxidation pathway. The rates of $OH\cdot$-derived alkoxy bond scissions were thus calculated for reference, in case their products would be detected in significant proportions. Nevertheless, $OH\cdot$ concentration in the chamber was quenched with a scavenger to enhance the detectability of the ozonolysis products. The mechanisms of these oxidation reactions are presented in Figures 5.4, 5.5 and 5.6, and the rates of the corresponding alkoxy bond scissions are presented in Table 5.1. The $OH\cdot$-oxidation of Isobutenamine is especially notable, as oxidation of the amine group is not only possible, but also competitive with oxidation of the double bond. [7],[52] This is all the more reason to limit the concentration of $OH\cdot$ in the chamber.

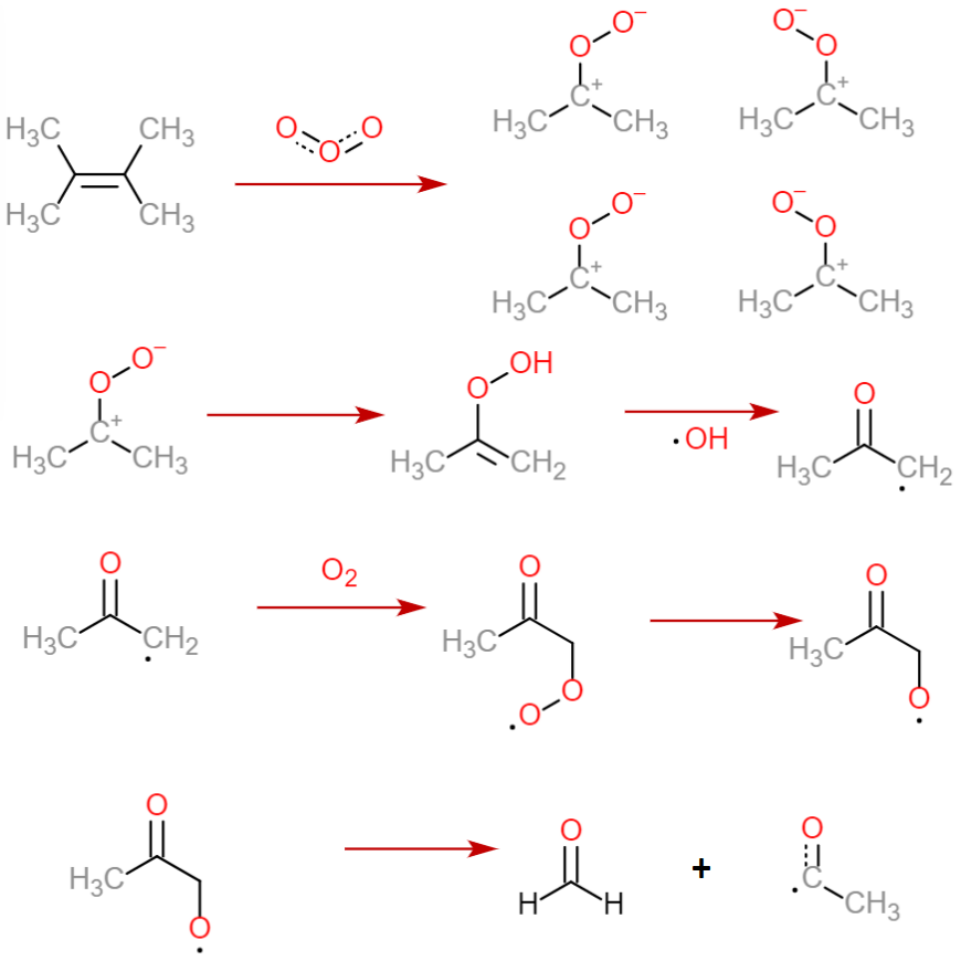

Figure 5.1: Reaction mechanism for Ozonolysis of TME. The symmetry around the C=C-bond means that all of the formed Criegee Intermediates are identical, and thus all are potential peroxy radical precursors. Very convenient. The bond scission rate, as presented in Table 4.5, is $k_S = 5{,}74 * 10^{10}$ s^{-1}.

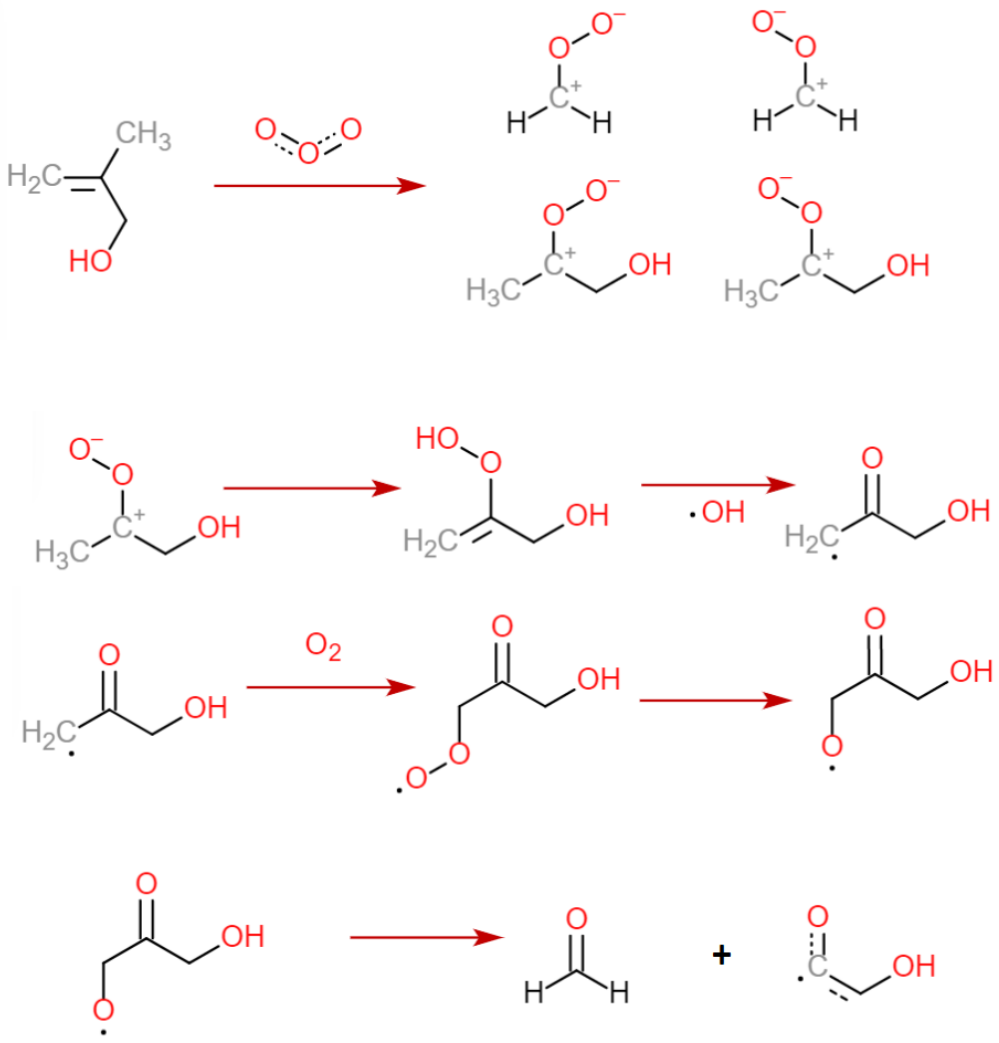

Figure 5.2: Reaction mechanism for Ozonolysis of Isobutenol. Out of the four formed Criegee Intermediates, only one has fast H-shift reaction. (The hydroxy-substituted CI may have one two, but this is unknown at the time of writing). The formed alkoxy radical is not found in any of the tables in Chapter 4, so it was calculated separately using the same procedure. The reaction turned out to have a submerged barrier ($E = -2{,}96 \frac{\text{kJ}}{\text{mol}}$), with an exact rate of $k_S = 3{,}16 * 10^{13}$ s^{-1}.

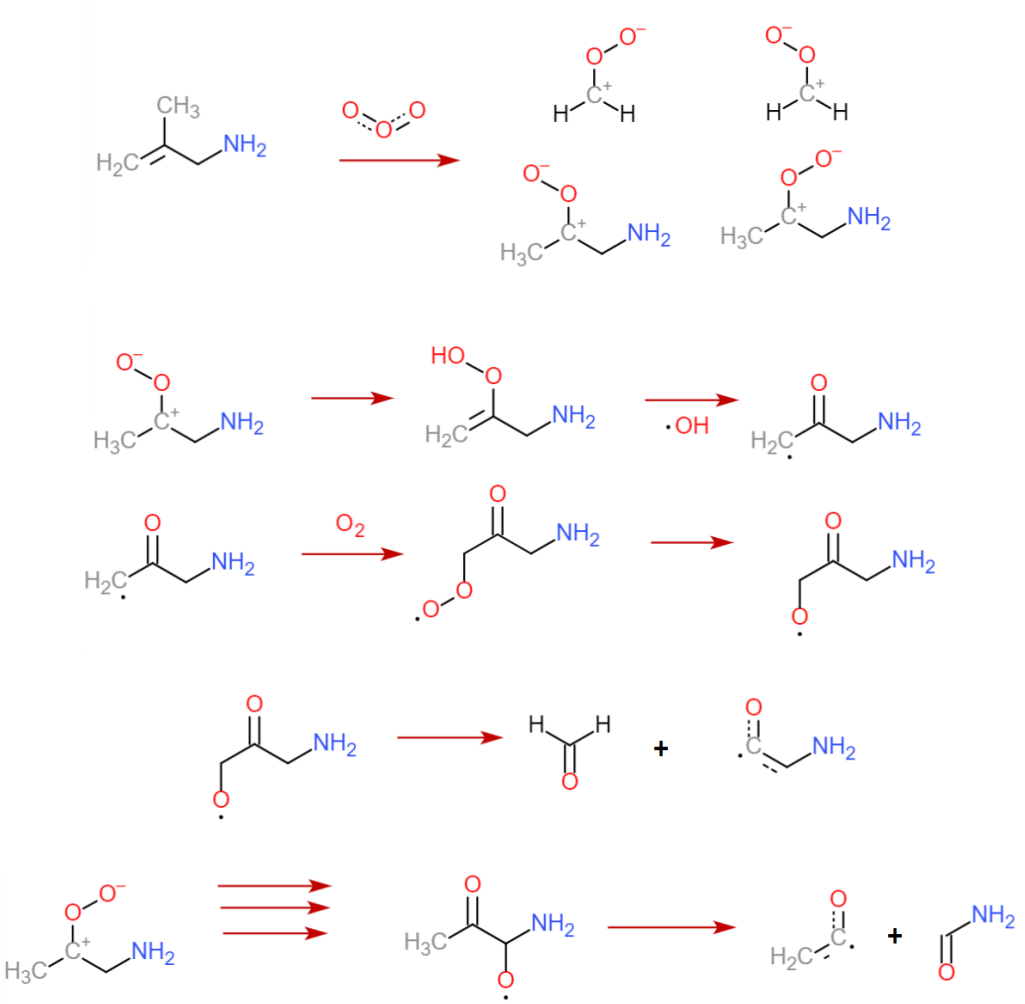

Figure 5.3: Reaction mechanism for Ozonolysis of Isobutenamine. Here, two of the the Criegee Intermediates are potential peroxy radical precursors. Both alkoxy bond scission rates are very rapid, the one shown above having a rate of $k_S = 3{,}16 * 10^{11}$ s^{-1} (Table 4.6), and $k_S = 5{,}55 * 10^{12}$ s^{-1} (assumed based on the barrierless $\alpha - \mathrm{NH_2}$-reaction in Table 4.6.)

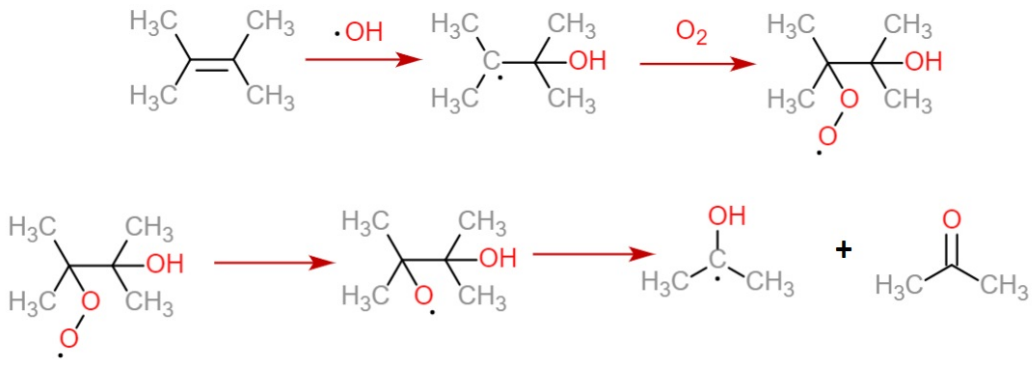

Figure 5.4: Reaction mechanism for OH· oxidation of TME. The calculated bond scission rate for the formed alkoxy radical is $k_S = 9{,}894 * 10^8$ s^{-1}.

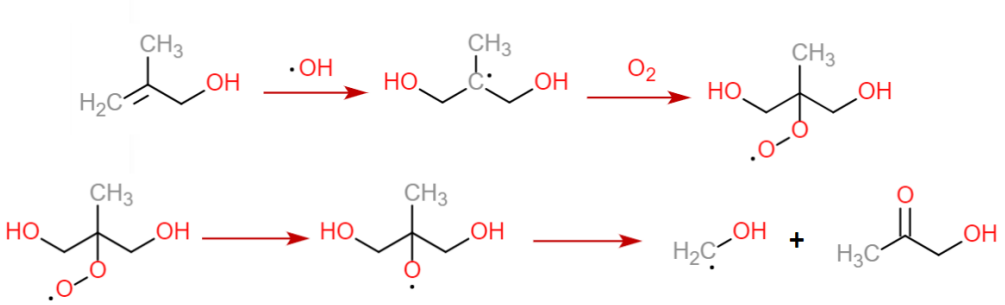

Figure 5.5: Reaction mechanism for OH· oxidation of Isobutenol. The calculated bond scission rate for the formed alkoxy radical is $k_S = 1{,}317 * 10^{10}$ s^{-1}.

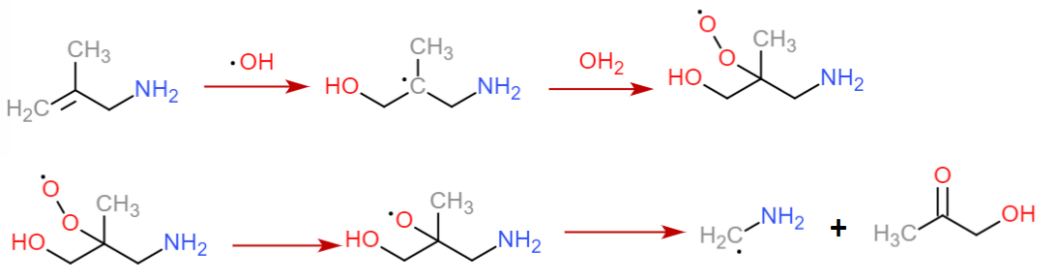

Figure 5.6: Reaction mechanism for OH· oxidation of Isobutenamine. Table 4.8 shows that the presented bond scission ought to be barrierless, so the rate was assumed to be in the order of 10^{13} s^{-1}.

5.2 Experimental Setup

The reactor in the COALA chamber is a 2 m^3 teflon bag shielded from light to better control the photochemistry. The reactor is connected to several flow tubes, and the gases are mixed in the chamber by fan. Pressure inside the chamber was roughly 1 atm during all of the experiments. The ambient air in the chamber consisted of outside air cleaned from excess aerosol particles and NO_x as well as from the most reactive organic pollutants. As we have already covered in Chapter 2.2, peroxy radicals react with NO_x, so keeping these concentrations low was extra important. For that reason, NO and NO_2 concentrations were monitored in real time during the experiments. The same air was used as the dilute gas of all gas flow going through the chamber. Alkene reactants are injected into the chamber using syringe pumps, slowly (at liquid-phase injection rates on the order of 50 nl/min) to make sure that all the substance exiting the syringe gets vaporized, ensuring that the concentration of alkene in the chamber is directly proportional to the injection rate. Both of the syringes were directly injected into a 300 ml/min flow, which was further diluted with a 5000 ml/min flow of the same air before entering the chamber. Ozone is created photolytically, by photolyzing O_2 at wavelengths below 310 nm. As per the Chapman mechanism, this should produce atomic Oxygen which then recombines with O_2, forming Ozone [53]. The photolyzed air is flown into the reactor at 5000 ml/min. In addition to the gas flows already mentioned, a 25000 ml/min flow of synthetic air was flown into the chamber to keep the exchange of gas inside the chamber relatively fast; when the volume of the chamber is divided by the total flow rate of 40,6 l/min, we see that the gas in the chamber is exchanged on average every 50 minutes. A simplified schematic of the chamber in its totality is shown in Figure 5.7.

Formed products are detected using NO_3^--CIMS-APi-TOF. TOF is the mass analysis method shown to be most compatible with time-resolved measurements, due

to its short spectrum acquisition time [54]. NO_3^--CIMS was the chosen ionization technique, as it has already been extensively used for HOM detection, and has been empirically shown to be very suitable for that purpose. [55] Quantum chemical calculations on (NO_3^-)(HOM)-cluster formation have shown that the explanation for this effect most likely lies in the electron withdrawing nature of the oxygen-containing functionalities leading to a strong affinity for hydrogen bonds. [56] Hydroperoxide-including HOMs are particularly prone to form (NO_3^-)(HOM)-clusters. In Chapter 1, we briefly touched on a reaction mechanism responsible for rapid formation of hydroperoxide functionalities in peroxy radicals, namely auto-oxidation [5]. This relates to the reason why cyclohexene was chosen as a partner molecule for the chamber oxidation. The peroxy radical formed in the ozonolysis of cyclohexene auto-oxidizes very rapidly, forming highly oxidized $C_6H_{10}O_9\cdot$-radicals within a span of seconds. This leads to the formation of HOMs with a high thermodynamic affinity for (NO_3^-)(HOM)-clusters, and therefore have a high detectability in the mass spectra. [57]

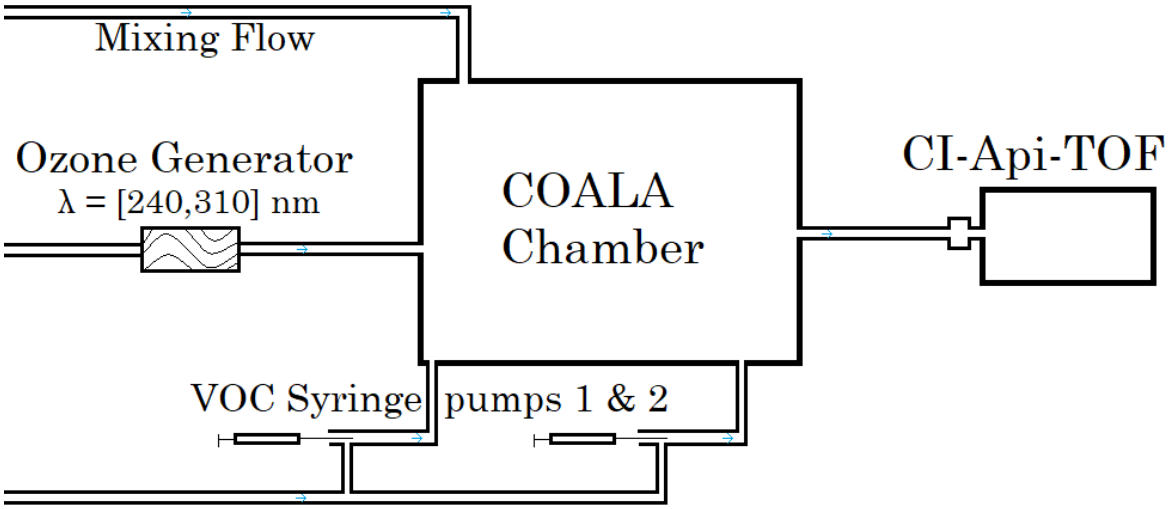

Figure 5.7: A simplified schematic of the experimental setup. The dilution flows for the VOC injections are omitted from the picture for simplicity.

The experiments were conducted separately for all three precursor alkenes. The mass spectra measurements were initiated with a short measurement of the background signal, after which cyclohexene injection was started at a rate corresponding to a mixing ratio of 60 ppb in the chamber. This injection rate was kept for the entire duration of the measurements. Simultaneously CO flow into the chamber was initiated at a rate deemed suitable for $OH\cdot + CO$ to be the main sink reaction for OH radicals. The injection rate chosen were the one corresponding to the mixing ratio of 50 ppm for the TME measurements and 100 ppm for the Isobutenol and Isobutenamine measurements (see Chapter 5.3, particularly Table 5.1 for the motivation for these rates). Once the concentrations of the relevant compounds in the chamber has stabilized, the mixing ratio of the second alkene was increased stepwise from 0 ppb to 60 ppb with a step size of 20 ppb. Due to the calculated average air exchange time of 50 minutes, the relaxation to a new steady state after an increase in injection rate was assumed to last around 70 minutes. After relatively steady concentrations had been confirmed from the signal of a known dimer, the alkene injection rate was increased to the next data point after an extra 15 minutes of waiting.

5.3 Dimerisation Kinetics in the COALA Chamber

In Chapter 2, we covered what is currently known on the mechanism of $ROO\cdot$ dimerisation. In this chapter, we will apply this knowledge to derive the concentration of the existing dimers in the chamber as a function of all variables we have the power to control, as a reference for the observed results. In this chapter, we will use the notation A and B to refer to generic peroxy radicals, to distinguish *self-dimers* formed from two identical radicals and *cross-dimers* formed from two different radicals.

The rate of change of the concentration of a generic dimer depends on its formation rate and of the loss rate in the chamber, determined to be on the order of

$k_{loss} = 2{,}5 * 10^{-3}$ s^{-1} in earlier published experiments in the same chamber [58]. From this we can solve an equilibrium concentration using the *pseudo-steady-state approximation.*

$$\frac{\mathrm{d}[\mathrm{ROOR_{AB}}]}{\mathrm{d}t} = k_{AB}[\mathrm{ROO_A}\cdot][\mathrm{ROO_B}\cdot] - k_{loss}[\mathrm{ROOR_{AB}}] \approx 0 \tag{5.1a}$$

$$[\mathrm{ROOR_{AB}}] \approx \frac{k_{AB}}{k_{loss}}[\mathrm{ROO_A}\cdot][\mathrm{ROO_B}\cdot] \tag{5.1b}$$

As we already covered in Chapter 2, the rate-limiting step of k_{AB} precedes the formation of the $(\mathrm{RO}\cdot + \mathrm{RO}\cdot)$ complex. This means we have no easy way of estimating it, and therefore neither $[\mathrm{ROOR_{AB}}]$. This will be kept in mind going forward. Nevertheless, let us use the same approach to derive an expression for the equilibrium concentration for a generic peroxy radical:

$$\frac{\mathrm{d}[\mathrm{ROO_A}\cdot]}{\mathrm{d}t} = k_{Ox}[\mathrm{Alk}][\mathrm{Ox}] - k_{AA}[\mathrm{ROO_A}\cdot]^2 - \sum_{i=1}^{n} k_{Ai}[\mathrm{ROO_A}\cdot][\mathrm{ROO_i}\cdot] \approx 0$$

$$[\mathrm{ROO_A}\cdot] = \frac{\sqrt{(\sum k_{Ai}[\mathrm{ROO_i}\cdot])^2 + 4k_{AA}k_{Ox}[\mathrm{Alk}][\mathrm{Ox}]} - \sum k_{Ai}[\mathrm{ROO_i}\cdot]}{2k_{AA}}$$

where [Alk] is the concentration of the precursor alkene, [Ox] is Ozone or $\mathrm{OH}\cdot$, and k_{Ox} the rate of oxidation. Other sink terms were assumed to be negligible, as NO_x had already been removed from the ambient air in the chamber. Next, let's use this to derive the concentration of self- and cross-dimers in the chamber. For self-dimers:

$$[\mathrm{ROOR_{AA}}] = \frac{k_{AA}}{k_{loss}}[\mathrm{ROO_A}\cdot]^2$$

$$= \frac{k_{Ox}}{k_{loss}}[\mathrm{Alk}][\mathrm{Ox}] + \frac{(\sum k_{Ai}[\mathrm{ROO_i}\cdot])^2}{2k_{AA}k_{loss}} - \frac{\sum k_{Ai}[\mathrm{ROO_i}\cdot]\sqrt{(\sum k_{Ai}[\mathrm{ROO_i}\cdot])^2 + 4k_{AA}k_{Ox}[\mathrm{Alk}][\mathrm{Ox}]}}{k_{loss}}$$

As we see, $[\mathrm{ROOR_{AA}}]$'s dependence on [Alk] can be anything from approximately linear to approximately proportional to the square root, depending on the relative rates of oxidation and dimerization. With good luck, the concentration approximates to

$[\mathrm{ROOR_{AA}}] \approx \frac{\mathrm{k_{Ox}}}{\mathrm{k_{loss}}}[\mathrm{Alk}][\mathrm{Ox}]$.

For cross-dimers, the equation is somewhat more complex:

$$
\begin{aligned}
[\mathrm{ROOR_{AB}}] &= \frac{k_{AB}}{k_{loss}}[\mathrm{ROO_A}\cdot][\mathrm{ROO_B}\cdot] \\
&= \frac{k_{AB}\left(\sqrt{(k_{AB}[\mathrm{ROO_B}\cdot] + \sum k_{Ai}[\mathrm{ROO_i}\cdot])^2 + 4k_{AA}k_{Ox}[\mathrm{Alk_A}][\mathrm{Ox}]} - k_{AB}[\mathrm{ROO_B}\cdot] - \sum k_{Ai}[\mathrm{ROO_i}\cdot]\right)}{2k_{loss}k_{AA}} \\
&* \frac{k_{AB}\left(\sqrt{(k_{AB}[\mathrm{ROO_A}\cdot] + \sum k_{Bi}[\mathrm{ROO_i}\cdot])^2 + 4k_{BB}k_{Ox}[\mathrm{Alk_B}][\mathrm{Ox}]} - k_{AB}[\mathrm{ROO_A}\cdot] - \sum k_{Bi}[\mathrm{ROO_i}\cdot]\right)}{2k_{loss}k_{BB}}
\end{aligned}
$$

A very complicated equation, which does not bend itself easily to a linear framework, except in pseudo-first order conditions where $k_{AB}[\mathrm{ROO_A}\cdot]$ overwhelms all other terms in the equation. However, concentrations of low-volatility compounds in the chamber were generally kept low to prevent contamination of future measurements.

The O_3 mixing ratio was monitored directly in the COALA chamber, but the $\mathrm{OH}\cdot$ mixing ratio wasn't. However, we can use the pseudo-steady state approximation to estimate $[\mathrm{OH}\cdot]$ in order to determine what flow rate of CO is needed to quench the competing oxidation pathway. For the PSSA, we assume that all $\mathrm{OH}\cdot$ is formed through VHP dissociation and consumed either in reactions with either CO or either precursor alkene in the chamber.

$$
\begin{aligned}
&\frac{\mathrm{d}[\mathrm{OH}\cdot]}{\mathrm{d}t} = k_A[\mathrm{VHP_A}] + k_B[\mathrm{VHP_B}] - k_{\mathrm{OHA}}[\mathrm{OH}\cdot][\mathrm{Alk_A}] - k_{\mathrm{OHB}}[\mathrm{OH}\cdot][\mathrm{Alk_B}] - k_{\mathrm{CO}}[\mathrm{OH}\cdot][\mathrm{CO}] \approx 0 \\
&\rightarrow [\mathrm{OH}\cdot] \approx \frac{k_A[\mathrm{VHP_A}] + k_B[\mathrm{VHP_B}]}{k_{\mathrm{OHA}}[\mathrm{Alk_A}] + k_{\mathrm{OHB}}[\mathrm{Alk_B}] + k_{\mathrm{CO}}[\mathrm{CO}]} = [\mathrm{O_3}]\frac{k_{\mathrm{O_3A}}[\mathrm{Alk_A}] + k_{\mathrm{O_3B}}[\mathrm{Alk_B}]}{k_{\mathrm{OHA}}[\mathrm{Alk_A}] + k_{\mathrm{OHB}}[\mathrm{Alk_B}] + k_{\mathrm{CO}}[\mathrm{CO}]}
\end{aligned}
$$

Where we on the last row have again assumed a stedy state for the VHP concentrations, knowing that the ozonolysis reaction is much slower than the barrierless VHP dissociation. To maximize the concentration of the dimers we actually hoped to see, [CO] was kept four orders of magnitude higher than either $[\mathrm{Alk_A}]$ or

Table 5.1: Used bimolecular reaction rates for estimation of OH· concentration during the experiments. The impact of alcohol and amine groups on the bimolecular reaction rates was assumed to be small. The relative rates of the OH· oxidation reactions are the reason for the chosen CO concentrations in the chamber.

Reaction	Rate ($\frac{cm^3}{smolec.}$)	Source	Source type
OH· + CO	2,44E-13	[59]	Experimental
OH· + c−hex	5,61E-11	[7]	SAR, OH· + cis-alkene
OH· + TME	1,10E-10	[7]	SAR, OH·+ > C=C <
OH· + Isobutenol	8,69E-11	[7]	SAR, OH· + Allyl
OH· + Isobutenamine	8,69E-11	[7]	SAR, OH· + Allyl
O_3 + c−hex	8,10E-17	[60]	Experimental
O_3 + TME	1,24E-15	[61]	SAR, O_3+ > C=C <
O_3 + Isobutenol	2,40E-17	[61]	SAR, O_3 + Allyl
O_3 + Isobutenamine	2,40E-17	[61]	SAR, O_3 + Allyl

$[Alk_B]$. This was necessary, as the bimolecular rate constant of the CO reaction is $k_{CO} = 2{,}436 * 10^{-13} \frac{cm^3}{molec.\ s}$ according to the experimental results of McCabe *et.al.*, [59], two levels of magnitude slower than other OH· reactions. These rates are summed up along with their sources in Table 5.1.

5.4 Results and Discussion

Analysis of the mass spectra was done using TOFware, an IGOR-based commercial software by Aerodyne Research. Mass calibration and mass peak shape fitting was done using the NO_3^-, $(HNO_3)NO_3^-$ and $(HNO_3)_2NO_3^-$ peaks present in every NO_3^--CIMS spectra as reference peaks. The resulting peak shape fit was implemented on all signals at the masses of the $(HOM)(HNO_3)_n(NO_3-)$ -clusters of the expected $ROOR_{AA}$,

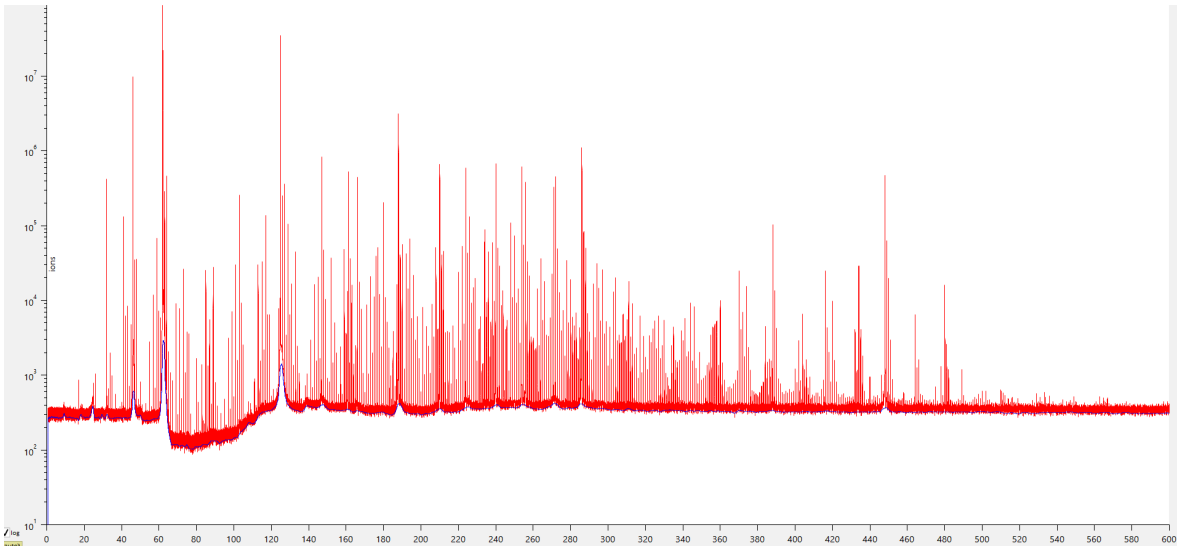

Figure 5.8: A typical time-averaged mass spectra in logarithmic scale.

ROR_{AA}', $ROOR_{AB}$, and ROR_{AB}'-dimers formed from ozonolysis. Signals from $OH\cdot$-oxidation were looked into as well, but none of the signals were significant, which can be interpreted as a sign that the scavenging was successful.

A short note on the fit curves seen in the figures below: The measured signal is displayed in red, and the fitted signal in blue. The green curve represents isotope peaks from characterized compounds in a peak one mass unit smaller, in cases where said peak had a higher signal than the one we were hoping to characterize. The black curve represents the remaining fits, that is, the fits for the compounds displayed in the picture.

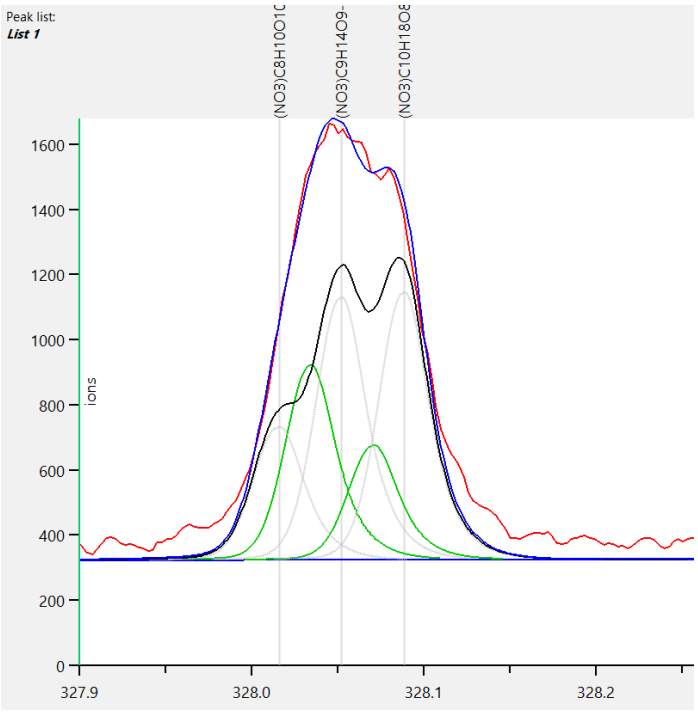

Figure 5.9: Mass peak from the cross dimer of TME and cyclohexene ($(NO_3^-)C_9H_{14}O_9$), with most byproducts characterized.

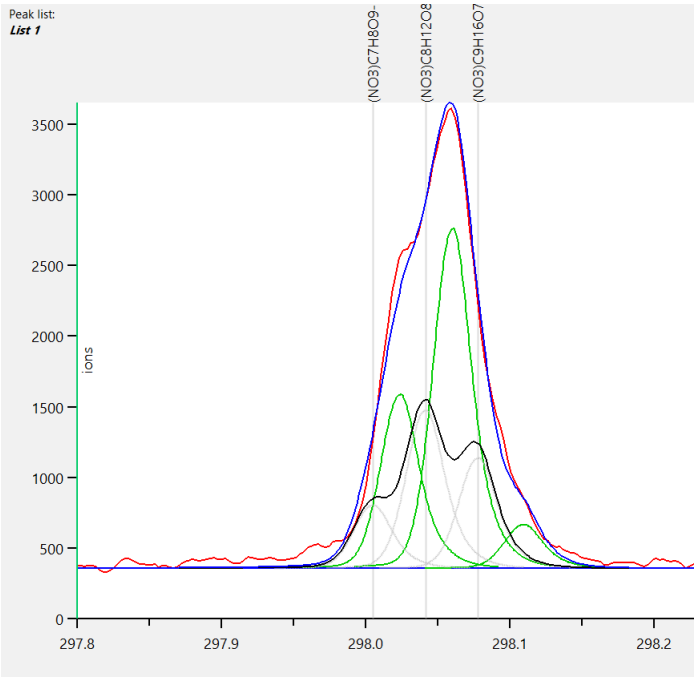

Figure 5.10: Mass peak from the scissioned cross dimer of TME and cyclohexene ($(NO_3^-)C_8H_{12}O_8$).

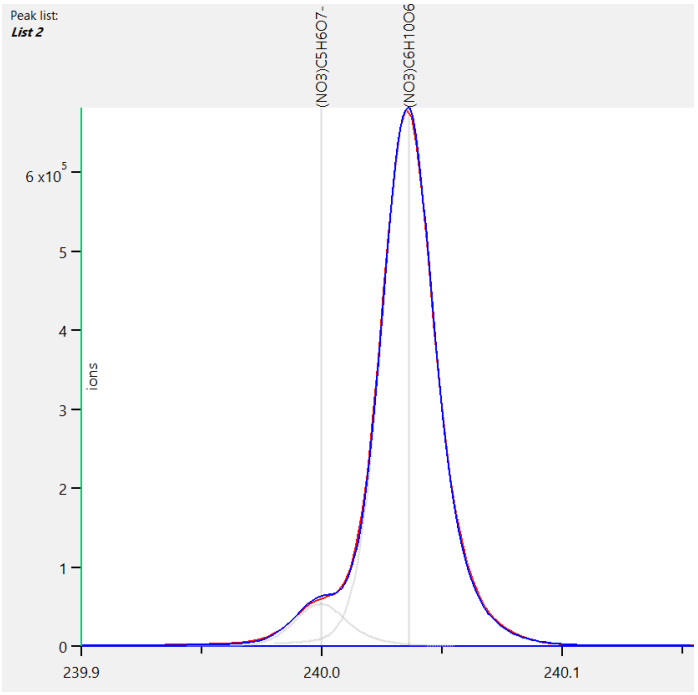

Figure 5.11: Mass peak from the self dimer of Isobutenol ($(NO_3{}^-)C_6H_{10}O_6$).

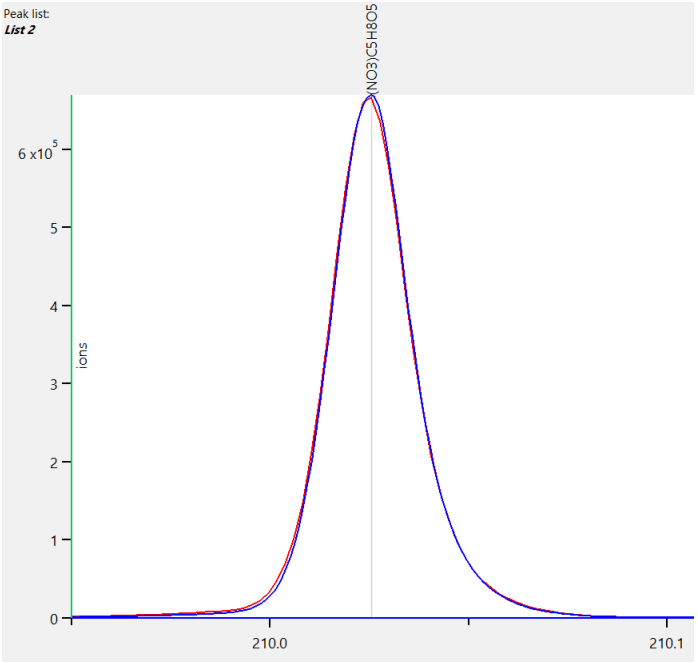

Figure 5.12: Mass peak from the scissioned self dimer of Isobutenol.

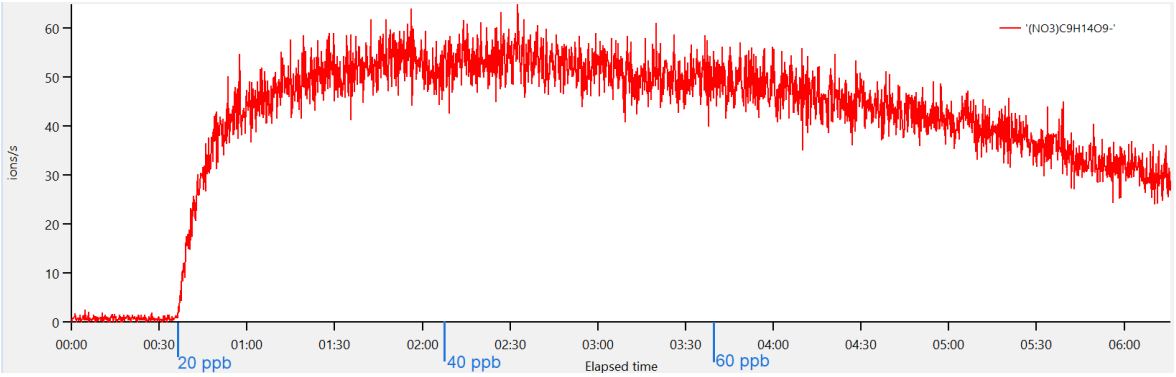

Figure 5.13: The time series of the TME+Cyclohexene ROOR cross-dimer signal. Times at which the TME injection was started or increased are marked in blue. The decrease in signal strength observed when TME precursor was added is most likely due to a decreased production of $C_6H_{10}O_9 \cdot$ radicals. As seen from Table 5.1, the TME ozonolysis is considerably faster than cyclohexene ozonolysis.

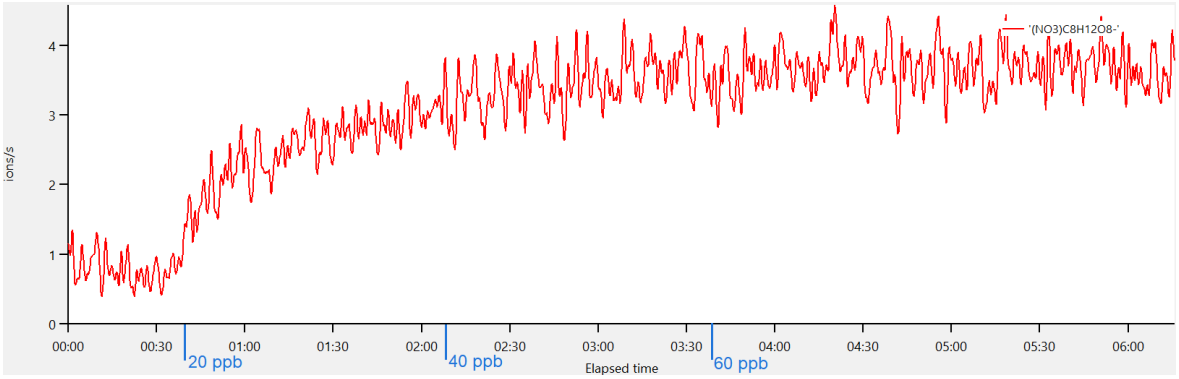

Figure 5.14: The time series of the corresponding ROR′ dimer, clearly showing that the dimers are indeed produced when TME precursor is added.

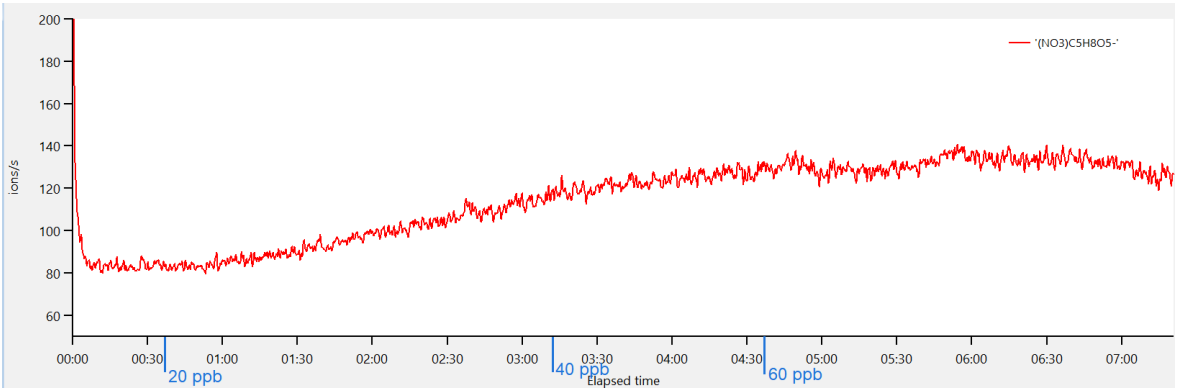

Figure 5.15: The scissioned ROR′ product of the Isobutenol self-dimer. These results are less unambiguous than for the TME ROR′. The high signal baseline is most likely due to a cyclohexene monomer with the same chemical composition, and the slow signal growth might be attributed to the accumulation of said monomer on the surfaces of the chamber and the pipes leading up to the spectrometer. There might be a small ROR′ in there, but it is difficult to determine conclusively from this data. Furthermore, the signal from the scissioned cross-dimer was quite small, on the order of 1-3 ions/s.

In summary, from the TME experiment we see clear evidence of ROR′ dimer formation, while in the Isobutenol experiment the results probably require somewhat larger precursor concentrations to make conclusions. Furthermore, the signal is one order of magnitude weaker that the corresponding ROOR signal, which possibly suggests that k_{ISC} is faster than k_S for this particular system, but we do not have enough information to verify or refute this information. For Isobutenamine, all the relevant signals were quite weak, and the time-dependence of the signals barely noticeable. One possible explanation for this is that OH$\cdot$ oxidation of the amine group dominated over the ozonolysis, but no significant production of NO_x was observed in the chamber during the experiment, so the more likely explanation is that neither ROOR nor ROR′ formation is significant for Isobutenamine.

Now, the next question is, can we determine an experimental rate for k_{ISC} using

these results, since we already have a precise computational result for k_S and observable results for both products? In theory, this ought to be possible, as the relative formation rate of the two dimers corresponds to the reaction rates.

$$\frac{k_{ISC}}{k_S} = \frac{[\mathrm{ROOR}]}{[\mathrm{ROR}']} \tag{5.6}$$

Earlier chamber experiments by Ehn *et.al.* and Jokinen et.al. derived a way to determine the concentration of oxidation products based on the mass spectra signals [62],[63]:

$$[\mathrm{X}] = C_X \frac{\sum_{i=0}^{2} \left[(\mathrm{HNO_3})_i(\mathrm{NO_3}^-)(\mathrm{X}) + (\mathrm{HNO_3})_i(\mathrm{X{-}H})^-\right]}{\sum_{i=0}^{2} (\mathrm{HNO_3})_i(\mathrm{NO_3}^-)} \tag{5.7}$$

where C_X is a calibration factor that needs to be determined separately. In our data, the signals of the nitric acid-including clusters were an order of magnitude lower than the corresponding $(\mathrm{NO_3}^-)(\mathrm{X})$ cluster, meaning that equation 5.6 approximates to:

$$\frac{[\mathrm{ROOR}]}{[\mathrm{ROR}']} \approx \frac{C_{\mathrm{ROOR}}}{C_{\mathrm{ROR}'}} \frac{(\mathrm{NO_3}^-)(\mathrm{ROOR})}{(\mathrm{NO_3}^-)(\mathrm{ROR}')}$$

where we may further approximate $C_{\mathrm{ROOR}} \approx C_{\mathrm{ROR}'}$, as the affinity for nitrate complex formation should barely differ between the two molecules. From the resulting function, a k_{ISC} could theoretically be determined by observing how the two signals are effected by the rise of precursor alkene. But alas, as we see from Figures 5.13 to 5.15, our signal strength as a function of time (or physically, as a function of the alkene concentration) behaves non-linearly, which means that fitting a function to it isn't easy. To an extent this is to be expected, as seen from the equation derived in Chapter 5.3. If this kind of study were attempted, the experimental conditions ought to be fixed to make [ROOR]([Alk)] and [ROR′]([Alk)] behave roughly linearly. At least for this combination of molecules, this might prove difficult in practise.

6. Conclusions

Our computational studies on the alkoxy bond scission rates for likely alkoxy intermediates suggest that the ROR formation pathway might prove to be competitive for many atmospherically relevant systems. From our experimental results we were able to conclude that the mechanism does result in ROR′ formation for at least one molecule with a computationally rapid alkoxy bond scission ($5{,}74 * 10^{10}$ s^{-1}). This molecule is acetyl peroxy radical, or $CH_3COCH_2OO\cdot$. We do not, however have the competing reaction rates for the ($C_3H_5O_2\cdot + C_6H_9O_7\cdot$) system, so we are not able to do quantitative comparisons with the current information. As mentioned in Chapter 5.4, experimental ROOR formation rates could also be determined for some systems with precise selection of experimental conditions. That said, the difference in signal strength between the (NO_3^-)(ROOR) and (NO_3^-)(ROR′) signals suggests either that k_{ISC} is an order of magnitude faster than k_S for the ($C_3H_5O_2\cdot + C_6H_9O_7\cdot$) pair, or that not all alkoxy bond scissions within a suitable distance lead to ROR′ formation.

Either way, now that the possibility of alkoxy bond scission-controlled ROR formation is confirmed as a possibility, the natural next step would be an extensive quantitative comparison of either reaction rates or product yields to determine for which peroxy radical systems the pathway is of any importance. As already noted at the end of Chapter 4, peroxy radicals formed from the ozonolysis of alkenes with long carbon chains are a good place to start, as they have very rapid alkoxy bond scissions by

default.

Bibliography

1 M. Shrivastava, C. D. Cappa, J. Fan, A. H. Goldstein, A. B. Guenther, J. L. Jimenez, C. Kuang, A. Laskin, S. T. Martin, N. L. Ng, T. Petaja, J. R. Pierce, P. J. Rasch, P. Roldin, J. H. Seinfeld, J. Shilling, J. N. Smith, J. A. Thornton, R. Volkamer, J. Wang, D. R. Worsnop, R. A. Zaveri, A. Zelenyuk and Q. Zhang, Reviews of Geophysics, 2017, **55**, 509–559.

2 M. Kanakidou, J. H. Seinfeld, S. N. Pandis, I. Barnes, F. J. Dentener, M. C. Facchini, R. Van Dingenen, B. Ervens, A. Nenes, C. J. Nielsen, E. Swietlicki, J. P. Putaud, Y. Balkanski, S. Fuzzi, J. Horth, G. K. Moortgat, R. Winterhalter, C. E. L. Myhre, K. Tsigaridis, E. Vignati, E. G. Stephanou and J. Wilson, Atmospheric Chemistry and Physics, 2005, **5**, 1053–1123.

3 H. Gordon, J. Kirkby, U. Baltensperger, F. Bianchi, M. Breitenlechner, J. Curtius, A. Dias, J. Dommen, N. Donahue, E. Dunne, J. Duplissy, S. Ehrhart, R. Flagan, C. Frege, C. Fuchs, A. Hansel, C. Hoyle, M. Kulmala, A. Kurten, K. Lehtipalo, V. Makhmutov, U. Molteni, M. Rissanen, Y. Stozkhov, J. Trostl, G. Tsagkogeorgas, R. Wagner, C. Williamson, D. Wimmer, P. Winkler, C. Yan and K. Carslaw, Journal of Geophysical Research: Atmospheres, 2017, **122**, 8739–8760.

4 E. Öström, Z. Putian, G. Schurgers, M. Mishurov, N. Kivekäs, H. Lihavainen, M. Ehn, M. P. Rissanen, T. Kurtén, M. Boy, E. Swietlicki and P. Roldin, Atmospheric Chemistry and Physics, 2017, **17**, 8887–8901.

5 F. Bianchi, T. Kurtén, M. Riva, C. Mohr, M. P. Rissanen, P. Roldin, T. Berndt, J. D. Crounse, P. O. Wennberg, T. F. Mentel, J. Wildt, H. Junninen, T. Jokinen, M. Kulmala, D. R. Worsnop, J. A. Thornton, N. Donahue, H. G. Kjaergaard and M. Ehn, Chemical Reviews, 2019, **119**, 3472–3509.

6 L. Vereecken, D. R. Glowacki and M. J. Pilling, Chemical Reviews, 2015, **115**, 4063–4114.

7 R. Atkinson, Environmental Toxicology and Chemistry, 1988, **7**, 435–442.

8 J. Kerdouci, B. Picquet-Varrault and J.-F. Doussin, Chemphyschem : a European journal of chemical physics and physical chemistry, 2010, **11**, 3909–20.

9 R. Criegee, Angew. Chem., 1975, **14**, 745–751.

10 T. Kurten and N. Donahue, Journal of Physical Chemistry A, 2012, **116**, 6823–6830.

11 L. Vereecken, A. Novelli and D. Taraborrelli, Phys. Chem. Chem. Phys., 2017, **19**, 31599–31612.

12 P. D. Lightfoot, R. A. Cox, J. N. Crowley, M. Destriau, G. D. Hayman, M. E. Jenkin, G. K. Moortgat and F. Zabel, Atmospheric Environment. Part A. General Topics, 1992, **26**, 1805–1961.

13 J. D. Crounse, L. B. Nielsen, S. Jørgensen, H. G. Kjaergaard and P. O. Wennberg, The Journal of Physical Chemistry Letters, 2013, **4**, 3513–3520.

14 J. J. Orlando and G. S. Tyndall, Chem. Soc. Rev., 2012, **41**, 6294–6317.

15 D. Stone, L. K. Whalley and D. E. Heard, Chem. Soc. Rev., 2012, **41**, 6348–6404.

16 K. U. Ingold, Accounts of Chemical Research, 1969, **2**, 1–9.

17 G. A. Russell, Journal of the American Chemical Society vol. 79 iss. 14, 1957, **79**, 3871–3877.

18 E. M. Y. Quinga and G. D. Mendenhall, Journal of the American Chemical Society, 1983, **105**, 6520–6521.

19 R. Lee, G. Gryn'ova, K. U. Ingold and M. L. Coote, Phys. Chem. Chem. Phys., 2016, **18**, 23673–23679.

20 J. J. Orlando, G. S. Tyndall and T. J. Wallington, Chemical Reviews, 2003, **103**, 4657–4690.

21 O. Setokuchi and M. Sato, The Journal of Physical Chemistry A, 2002, **106**, 8124–8132.

22 O. Horie, J. N. Crowley and K. Moortgat, G, The Journal of Physical Chemistry, 1990, **94**, 8198–8203.

23 G. Ghigo, A. Maranzana and G. Tonachini, The Journal of Chemical Physics, 2003, **118**, 10575–10583.

24 S. Khursan, PATAI'S Chemistry of Functional Groups || Organic tetroxides and mechanism of peroxy radical recombination, John Wiley Sons, Ltd, 2014, pp. 1–34.

25 I. N. Levine, Quantum Chemistry, 6th edition, Pearson International Edition, 2009, pp. 322–343.

26 R. R. Valiev, G. Hasan, V.-T. Salo, J. Kubečka and T. Kurten, The Journal of Physical Chemistry A, 2019, **123**, 6596–6604.

27 J. N. Harvey, Phys. Chem. Chem. Phys., 2007, **9**, 331–343.

28 R. R. Valiev, V. N. Cherepanov, G. V. Baryshnikov and D. Sundholm, Phys. Chem. Chem. Phys., 2018, **20**, 6121–6133.

29 G. Hasan, V.-T. Salo, R. R. Valiev, J. Kubečka and T. Kurtén, The Journal of Physical Chemistry A, 2020, **124**, 8305–8320.

30 P. Aktins and J. De Paula, Atkins' Physical Chemistry, 10th edition, Oxford University Press, 2014, pp. 805–810, 889–898.

31 J. Crank, The Mathematics of Diffusion, Clarendon Press, 1975, pp. 2–4.

32 L. Vereecken and J. Peeters, Phys. Chem. Chem. Phys., 2009, **11**, 9062–9074.

33 C. Eckart, Phys. Rev., 1930, **35**, 1303–1309.

34 D. A. McQuarrie and J. D. Simon, Physical Chemistry: A Molecular Approach, University Science Books, 1997, pp. 693–716.

35 P. Y. Ayala and H. B. Schlegel, The Journal of Chemical Physics, 1998, **108**, 2314–2325.

36 H. Koskinen and R. Vainio, Klassinen Mekaniikka, Like, 2010, pp. 84–89, 120–125.

37 F. Jensen, Introduction to Computational Chemistry: Second Edition, Wiley, 2007, pp. 133–135,192–198.

38 A. Szabo and N. S. Ostlund, Modern Quantum Chemistry: Introduction to Advanced Electronic Structure Theory, Dover, 1996, pp. 46–60, 286–291, 320–327.

39 R. Ditchfield, W. J. Hehre and J. A. Pople, The Journal of Chemical Physics, 1971, **54**, 724–728.

40 M. J. Frisch, J. A. Pople and J. S. Binkley, The Journal of Chemical Physics, 1984, **80**, 3265–3269.

41 T. H. Dunning, The Journal of Chemical Physics, 1989, **90**, 1007–1023.

42 S. Ten-no, Chemical Physics Letters, 2004, **398**, 56–61.

43 W. Kohn and L. J. Sham, Phys. Rev., 1965, **140**, A1133–A1138.

44 J. P. Perdew and K. Schmidt, AIP Conference Proceedings, 2001, **577**, 1–20.

45 A. D. Becke, The Journal of Chemical Physics, 1993, **98**, 5648–5652.

46 C. Lee, W. Yang and R. G. Parr, Phys. Rev. B, 1988, **37**, 785–789.

47 A. D. Becke, Phys. Rev. A, 1988, **38**, 3098–3100.

48 J.-D. Chai and M. Head-Gordon, The Journal of Chemical Physics, 2008, **128**, 084106.

49 A. D. Becke, The Journal of Chemical Physics, 1997, **107**, 8554–8560.

50 J.-D. Chai and M. Head-Gordon, Phys. Chem. Chem. Phys., 2008, **10**, 6615–6620.

51 J. Peeters, G. Fantechi and L. Vereecken, J. Atmos. Chem., 2004, **48**, 59–80.

52 D. Lee and A. Wexler, Atmospheric Environment, 2013, **71**, 95–103.

53 J. H. Seinfield and S. N. Pandis, Atmospheric Chemistry and Physics: From Air Pollution to Climate Change, 2nd Edition, Wiley, 2006, pp. 142–151.

54 P. L. Urban, Y. C. Chen and Y.-S. Wang, Time-Resolved Mass Spectrometry: From Concepts to Applications, Wiley, 2016, pp. 54–57.

55 T. Jokinen, M. Sipilä, H. Junninen, M. Ehn, G. Lönn, J. Hakala, T. Petäjä, R. L. Mauldin III, M. Kulmala and D. R. Worsnop, Atmospheric Chemistry and Physics, 2012, **12**, 4117–4125.

56 N. Hyttinen, O. Kupiainen-Määttä, M. P. Rissanen, M. Muuronen, M. Ehn and T. Kurtén, The Journal of Physical Chemistry A, 2015, **119**, 6339–6345.

57 T. Berndt, S. Richters, R. Kaethner, J. Voigtländer, F. Stratmann, M. Sipilä, M. Kulmala and H. Herrmann, The Journal of Physical Chemistry A, 2015, **119**, 10336–10348.

58 O. Peräkylä, M. Riva, L. Heikkinen, L. Quéléver, P. Roldin and M. Ehn, Atmospheric Chemistry and Physics, 2020, **20**, 649–669.

59 D. C. McCabe, T. Gierczak, R. K. Talukdar and A. R. Ravishankara, Geophysical Research Letters, 2001, **28**, 3135–3138.

60 D. Stewart, S. Almabrok, J. Lockhart, O. Mohamed, D. Nutt, C. Pfrang and G. Marston, Atmospheric Environment, 2013, **70**, 227–235.

61 Standard Reference Database 17, 2007.

62 M. Ehn, J. A. Thornton, E. Kleist, M. Sipilä, H. Junninen, I. Pullinen, M. Springer, F. Rubach, R. Tillmann, B. Lee, F. Lopez-Hilfiker, S. Andres, I.-H. Acir, M. Rissanen, T. Jokinen, S. Schobesberger, J. Kangasluoma, J. Kontkanen, T. Nieminen, T. Kurtén, L. B. Nielsen, S. Jørgensen, H. G. Kjaergaard, M. Canagaratna, M. D. Maso, T. Berndt, T. Petäjä, A. Wahner, V.-M. Kerminen, M. Kulmala, D. R. Worsnop, J. Wildt and T. F. Mentel, Nature, 2014, **506**, 1476–4687.

63 T. Jokinen, M. Sipilä, H. Junninen, M. Ehn, G. Lönn, J. Hakala, T. Petäjä, R. L. Mauldin III, M. Kulmala and D. R. Worsnop, Atmospheric Chemistry and Physics, 2012, **12**, 4117–4125.